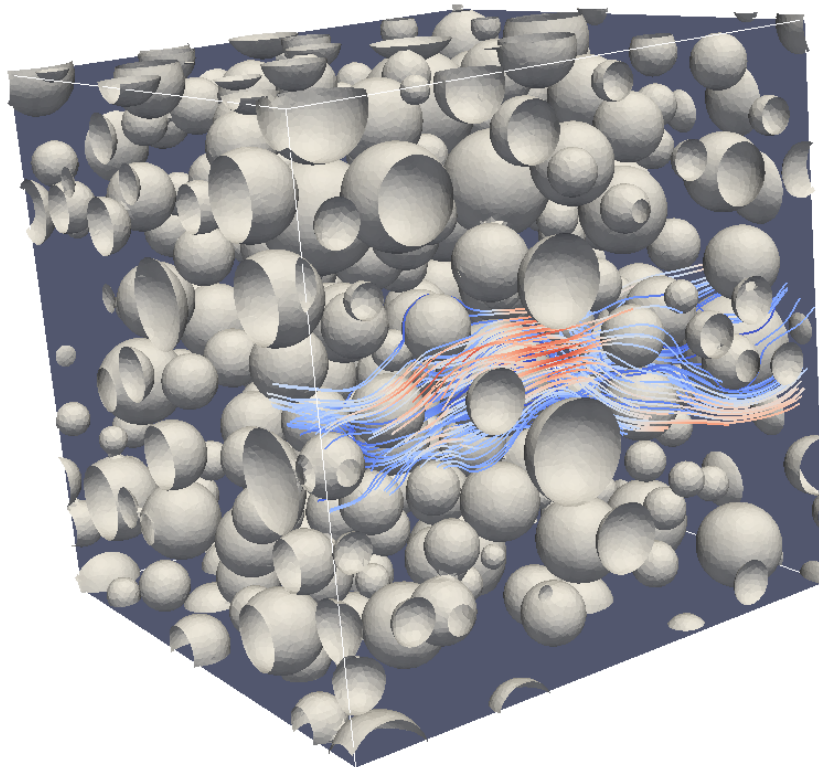




CHALMERS
UNIVERSITY OF TECHNOLOGY



Mass Transport in Heterogeneous Porous Granular Materials

Master's thesis in Complex Adaptive Systems

PETER SVENSSON

MASTER'S THESIS IN COMPLEX ADAPTIVE SYSTEMS

**Mass Transport in Heterogeneous Porous
Granular Materials**

PETER SVENSSON



CHALMERS
UNIVERSITY OF TECHNOLOGY

Department of Physics
CHALMERS UNIVERSITY OF TECHNOLOGY
Gothenburg, Sweden 2016

Mass Transport in Heterogeneous Porous Granular Materials
PETER SVENSSON

© PETER SVENSSON, 2016.

Supervisor: Magnus Röding, SP Food and Bioscience, Soft Materials Science
Examiner: Mats Granath, Department of Physics, University of Gothenburg

Department of Physics
Chalmers University of Technology
SE-412 96 Gothenburg
Telephone +46 31 772 1000

Cover: Fluid flow through a structure of solid volume fraction 0.20. The particle sizes are based on a lognormal distribution.

Mass Transport in Heterogeneous Porous Granular Materials
PETER SVENSSON
Department of Physics
Chalmers University of Technology

Abstract

In this thesis, the impact of the particle size distribution and spatial correlations in porous granular material structures on fluid permeability is systematically investigated. A goal is to complement the existing versions of the Kozeny-Carman equation, relating the material properties fluid permeability, porosity and specific surface, with an explicit spatial dependence. Including such a dependence would make it possible to distinguish between materials with different degree of heterogeneity, i.e. granular structures in which the granules are uniformly distributed and in which they tend to create clusters. An *in silico* (simulation-based) approach is employed, where virtual material structures based on monodisperse, lognormal and bidisperse size distributions of granules are generated using Monte Carlo-based algorithms. The spatial correlations in the structures are characterized using two types of microstructural descriptors, the pore size distribution and the two-point probability function. Fluid dynamics simulations, from which the fluid permeability is obtained, are performed using a lattice Boltzmann method-based software. The results suggest that there is a linear relationship between the fluid permeability and the squared mean of the pore size distribution. This relationship holds for isotropic structures. As the degree of isotropy decreases, the permeability becomes dependent on the flow direction. It is also shown that the two-point probability function may be used to investigate the order and correlations in the structures, as well as to characterize clustering.

Keywords: Virtual material design, fluid permeability, soft matter physics, granular media.

Acknowledgements

I would like to thank my supervisor Magnus Röding at SP Food and Bioscience and my examiner Mats Granath at University of Gothenburg for supervision, guidance and support. I would like to express my gratitude to the division Soft Materials Science at SP Food and Bioscience for providing this opportunity and for contributing to an inspiring atmosphere throughout the final phase of my master's studies. Finally, I would like to thank my loved ones for support and understanding throughout my years of studies.

Peter Svensson, Gothenburg, June 2016

Contents

List of Figures	xi
1 Introduction	1
1.1 Aim of the project	2
1.2 Method	2
1.3 Limitations	2
1.4 Outline	2
2 Theory	3
2.1 Material types	3
2.1.1 Soft matter	3
2.1.2 Porous and granular materials	3
2.2 Permeability	4
2.3 Models for granular materials and particle packings	5
2.4 Simulation techniques	8
2.4.1 Techniques for generating virtual material structures	8
2.4.2 Fluid flow modelling	8
2.5 Spatial statistics	10
2.5.1 Pore size probability density function	10
2.5.2 n -point probability function	10
2.6 Related earlier work	12
3 Methods	13
3.1 Generating virtual granular materials	13
3.1.1 Polydisperse size distribution	14
3.1.2 Lattice structures and random packings	15
3.1.3 Modifying the structure	16
3.1.3.1 Attractive force between particles	16
3.1.3.2 Attractive and repulsive forces between particles	17
3.1.3.3 Introducing repulsive point potentials in the domain	17
3.1.3.4 Selectively deleting one type of particle in structures	18
3.1.4 Triangulating the surface using VoxSurface	18
3.2 Mass transport simulations	19
3.2.1 The lattice Boltzmann method	19
3.2.2 Fluid dynamics simulations	20
3.3 Data analysis and spatial statistics	21

3.3.1	Calculating pore size distribution	21
3.3.2	Two-point probability function	21
3.3.3	Representation of the results	22
3.4	Simulation setup	23
3.4.1	Comparison of size distributions	23
3.4.2	The bidisperse size distribution	24
3.4.3	From lattice structures to random packings	25
3.4.4	Investigations of effects related to spatial correlations	25
4	Results and discussion	27
4.1	Comparison of size distributions	27
4.2	The bidisperse size distribution	30
4.3	From lattice structures to random packings	32
4.4	Investigation of effects related to spatial correlations	36
4.4.1	Introducing forces between particles	36
4.4.2	Repulsive point potentials	39
4.4.3	Deleting particles from the structure	43
4.5	The Kozeny-Carman equation	44
5	Conclusion	47
	Bibliography	49
A	Appendix 1	I
A.1	Statistical mechanics	I

List of Figures

2.1	Uniformly distributed particles (left) and clustered particles (right).	5
2.2	Cubic lattices. (a) is simple cubic, (b) is body-centred cubic, and (c) is face-centered cubic. In all cells, $\alpha = \beta = \gamma = \pi/2$ and $a = b = c$. Figure taken from [1].	6
2.3	Control volume $\delta V = \Delta x$ used in 1-D FVM. Figure taken from [2].	10
3.1	(a) An example of a generated structure after triangulation, coarsening and smoothing. The solid volume fraction is around 0.50 (0.493). As can be seen, portions of the particles that are located outside of the domain are cut off and moved to the corresponding opposite side of the volume. (b) Particles close to each other tend to get welded together in the discretization process.	19
3.2	A two dimensional example of adjacent lattice sites. Example taken from [3]	20
3.3	Example of two systems, nonoverlapping disks (upper) and overlapping disks (lower). The fractions of the two phases (disk and void) is 0.5. The disk diameter is D and the separation between the end points is r . The example is taken from [4].	22
3.4	A histogram of the scaled radii from the lognormal distribution. The volume fractions are scale independent, and the plot should merely function as a tool to display the spread in the distribution.	24
4.1	Permeability (left) and specific surface (right) for the monodisperse, lognormal and bidisperse size distributions as functions of the solid volume fraction. Note that l is the problem-dependent proper length (see Sections 3.3.3 and 3.4.1).	28
4.2	Mean pore sizes for the monodisperse, lognormal and bidisperse size distributions as functions of the solid volume fraction. Note that l is the problem-dependent proper length (see Sections 3.3.3 and 3.4.1).	28
4.3	Comparison between permeability and squared mean pore size for monodisperse, lognormal and bidisperse distributions as function of the solid volume fraction.	29
4.4	Permeability $[l^2]$ as a function of the number fraction (x-axes) of small particles plotted for all size ratios (captions) separately. The solid volume fraction is 0.50. Note that l is the problem-dependent proper length (see Sections 3.3.3 and 3.4.2)	31

4.5	The mean pore size $[l]$ as a function of the number fraction (x-axes) of small particles plotted for all size ratios (captions) separately. The solid volume fraction is 0.50. Note that l is the problem-dependent proper length (see Sections 3.3.3 and 3.4.2).	31
4.6	Comparison of permeability and squared mean pore size as a function of the number fraction (x-axes) of small particles plotted for all size ratios (captions) separately. The solid volume fraction is 0.50.	32
4.7	Permeability (left) and mean pore size (right) as functions of solid volume fraction. Note that l is the problem-dependent proper length (see Sections 3.3.3 and 3.4.3).	32
4.8	A comparison between the permeability and the squared mean pore size.	33
4.9	S_2 for the void phase as a function of the point separation for some different solid volume fractions.	34
4.10	The structures obtained by the lattice method (left) and RCP (right).	35
4.11	S_2 for the void phase as a function of the point separation for a solid volume fraction of 0.63, obtained by RCP and by the lattice method.	35
4.12	A comparison of the pore sizes for the two structures, obtained by RCP and by the lattice method. Note that l is the problem-dependent proper length (see Sections 3.3.3 and 3.4.3).	36
4.13	Permeability (left) and mean pore size (right) for the three different cases. Note that l is the problem-dependent proper length (see Sections 3.3.3 and 3.4.4).	37
4.14	A scaled comparison based on minimizing the sum of squared differences between permeability and squared mean pore size.	37
4.15	S_2 for the void phase for three cases (left) and a magnification of the minima (right). The solid volume fraction is 0.20.	38
4.16	S_2 for the void phase for three cases (left) and a magnification of the minima (right). The solid volume fraction is 0.22.	38
4.17	Specific surface as a function of the solid volume fraction for the original and the modified structures. Note that l is the problem-dependent proper length (see Sections 3.3.3 and 3.4.4).	39
4.18	Permeability (left) and mean pore size (right) as functions of the number of repulsive potentials and the solid volume fraction.	40
4.19	Comparison of the permeability and the squared mean pore size as a function of the solid volume fraction (x-axes) plotted separately for different number of repulsive potentials (captions). Note that l is the problem-dependent proper length (see Sections 3.3.3 and 3.4.4).	41
4.20	Comparison of two structures in the xy-plane for which the correspondence between the permeability and the squared mean pore size is good (left) and bad (right). The solid volume fraction is 0.22 in both cases, and the number of repulsive potentials is 48 (left) and 2 (right).	41

4.21	Same comparison as in Fig. 4.20, but from a different angle. The left structure produces a good correspondence and the right structure produces a bad correspondence. A clarification of the spatial orientation: x (red), y (green), z (blue).	42
4.22	S_2 for the two structures in Fig. 4.20 - 4.21.	42
4.23	Permeability (left) and mean pore size (right) as functions of number of larger particles and size ratio between the larger and smaller particles and solid volume fraction of the larger particles. Note that l is the problem-dependent proper length (see Sections 3.3.3 and 3.4.4). .	43
4.24	Comparison between the permeability and squared mean pore size as a function of the volume fraction of the larger particles, plotted separately for different size ratios.	44

1

Introduction

A prerequisite for technological progress overall is the development of novel materials tailored for certain purposes [5]. The materials development process involves experimental procedures where material samples are physically produced and tested, often in a costly and time-consuming trial-and-error manner [5, 6]. A material's functionality is the result of a combination of a number of structural properties and depends on the internal interactions between components. In order to understand and isolate individual material parameters, a decoupling of the complex interactions is needed [7, 8]. In addition, environmental toxicity and availability of natural resources need to be taken into account, making the developing process a task of a multiple dimensional nature [5]. A high-throughput experimental screening approach, where a systematic variation of parameters is performed in order to investigate the space of material structures, may in some cases imply a time span of development of many years, hindering the progress of technology [6]. Modern computational resources have opened up for new possibilities of virtual materials design and a digitalization of the high-throughput screening approach, where a combination of theoretical studies using computer simulations and experiments work symbiotically [6]. The need to produce physical samples is reduced, and instead computers function as virtual laboratories where material properties are investigated in a simulated environment. This approach is also beneficial in cases where the experimental procedures are difficult, one example being the search for stable alloys, where the production involves high pressures and temperatures and hazardous materials [5].

A vast field within materials science is soft materials, or soft condensed matter, which is a subfield of condensed matter [9]. Soft materials are complex structures including, among others, colloids, membranes, emulsions, a number of biomaterials, liquid crystals, and polymers. Some everyday examples are paint, glues, soaps and food. Many soft materials are porous, i.e. structures containing void parts. Depending on the void regions, or pores, and how these regions are connected inside the material, flow through the medium may be possible. A mathematical formulation relating the fluid permeability¹ of a material to microstructural features, e.g. porosity, is the Kozeny-Carman equation [10, 11]. However, a missing corner stone in the equation is an explicit dependence of the spatial distribution of the material components (or the pores). Spatial correlations are instead included in a constant, and hence it not possible to make an *a priori* distinction between materials possessing different degrees of heterogeneity. In order to facilitate better predictions of the permeability of porous media, a complement to the existing versions of the

¹From now on, *fluid permeability* and *permeability* will be used interchangeably.

Kozeny-Carman equation is needed.

1.1 Aim of the project

Systematic investigations using computer simulations will be performed to examine the link between different material structure parameters, such as different size distributions, and the permeability of porous materials. A pressure-driven flow will be employed. A goal is to find a property linked to the structure that can be used to complement an existing version of the Kozeny-Carman equation.

The project is performed at SP Food and Bioscience and is a part of the VINN Excellence Center SuMo Biomaterials collaboration at Chalmers University of Technology.

1.2 Method

The thesis is based on a theoretical approach, and no comparison to experimental data is performed. Virtual material structures are generated using Monte Carlo-based algorithms implemented in Matlab. Fluid dynamics simulations are performed using the lattice Boltzmann method-based software Gesualdo, developed as a part of the SuMo Biomaterials collaboration.

1.3 Limitations

There is a large number of material parameters to vary, e.g. the particle size distribution or the shape of the particles. Only granular materials consisting of spherical granules will be considered. It is assumed that the particles, or spheres, are impenetrable and, hence, nonoverlapping.

The Kozeny-Carman equation exists in different versions depending on the application. Only one version of the equation will be considered in this thesis.

There are several computational methods in order to generate virtual material structures, deterministic as well as stochastic. This project focuses on implementing stochastic Monte Carlo methods. No comparison between different generating methods is performed.

1.4 Outline

Chapter 2 begins with an introduction to different material types and material properties. Also, different simulation approaches are presented and some necessary mathematical preliminaries are dealt with. In Chapter 3, a more thorough explanation of the simulation methods most relevant to this project is presented, and the methods used in the simulations and the data analyses are explained. Chapter 4 combines results and discussion. Chapter 5 rounds off the thesis with some final concluding remarks and possible continuations.

2

Theory

2.1 Material types

2.1.1 Soft matter

A characteristic feature of materials which are to be accounted for as soft, is that they are neither typically crystalline solids nor liquids, seen from a mechanical point of view, where the response to an external force defines the division [9, 12]. Put simply, the most prominent characteristic is their macroscopic softness. An ideal Hookean solid will respond to a shear stress in a perfectly elastic way while a Newtonian fluid, which is the other of the two extreme behaviors of condensed matter, is characterized by its completely inelastic viscosity and will respond by producing a flow [12]. A soft material's response, on the other hand, is a combination of elastic and viscous behavior, a so called viscoelastic response, which is dependent on the time scale and the relaxation time of the system. If an external force is applied on a shorter time scale than the relaxation time, the viscoelastic soft material will behave as a solid, while in the opposite case the material will behave as a fluid [12]. An excellent example is a dispersion of corn starch in water, which will behave either as a solid or a fluid depending on the applied force (shear-thickening). Paint is another example, which will respond to an external force by getting thinner (shear-thinning) [12].

Some common features of soft materials are the importance of interactions on different length scales and the ability to self-assemble. Interactions on an atomic or molecular level may give rise to microscopic assemblies, which in turn may arrange in highly ordered larger structures and a hierarchical material [12]. An example of self-assembling systems are micelles, which are aggregations of amphiphilic molecules consisting of both an hydrophilic and an hydrophobic part. In an aquatic solution, the molecules create arrangements favorable for the amphiphile, like spheres or cylinders, where the hydrophobic parts are screened from the aquatic solution, and hence minimize the energy of the system [12].

2.1.2 Porous and granular materials

A porous material is a material that contains void regions, or pores. Due to the void type structure, porous materials have a larger specific area and possess a lighter weight compared to a more solid alternative, which may be desirable in certain applications. Porous structures are occurring both naturally, for example in bones, wood, corals and lava, and as industrially manufactured porous metals, porous ceramics and polymer foams [13]. A material property which works as a measure of

the void is porosity, which is defined as the fraction of the total volume in a medium that is occupied by pores. The relation between the volume fractions of void and solid is hence

$$\Phi_{void} + \Phi_{solid} = 1, \quad (2.1)$$

where Φ_{void} is the porosity and Φ_{solid} is the solid volume fraction. The pores in the material may be either isolated or connected, where connected pores contribute in the transport process, enabling for fluid to pass through the material [14]. A highly porous material lets fluid to pass more easily. Applications of flow through porous media are numerous, e.g. filtration or permeation of water [11].

Granular materials, such as collections of sand or rice, is a subgroup of porous materials. A granular material is composed of constituent particle, so-called granules. Due to the porous nature of the structures, granular materials are used in particle size separation processes, gel permeation chromatography and filtering, to name a few examples.

2.2 Permeability

Permeability characterizes a material's ability to let a flow of fluid pass through it. In 1856 [15], Darcy empirically established the law

$$\bar{v} = -\frac{\kappa \Delta p}{\mu L}, \quad (2.2)$$

where \bar{v} is the average flow velocity, κ is the permeability, μ is the dynamic viscosity, $L = |x_2 - x_1|$ is the length of the domain $[x_1, x_2]$ in the flow direction, and $\Delta p = p_2 - p_1$ is the pressure difference between x_1 and x_2 [16].

A frequently quoted empirical relation between the permeability, specific surface, i.e. the surface of the solid phase divided by the total volume of the domain, and porosity, is the Kozeny-Carman equation:

$$\kappa = C \frac{\Phi_{void}^3}{S^2(1 - \Phi_{void})^2}, \quad (2.3)$$

where κ is the permeability, C is a constant, Φ_{void} is the porosity, and S is the specific surface [11]. As can be seen, the permeability follows the intuition that a fully solid material with $\Phi_{void} = 0$ will not let any flow through, and the opposite situation, where a material only consists of void will let the fluid pass infinitely well. Note that both Darcy's law and the Kozeny-Carman equation are valid only for laminar flow, i.e. for small Reynolds numbers [11].

One would expect that the way materials are composed, i.e. if particles form clusters or tend to spread evenly, would have an effect on the permeability. However, as can be seen in Eq. (2.3), there is no dependence on the size of the voids. A measure of the void sizes is the material's pore size distribution, which is defined as the distribution of distances from all points in pore space to the nearest solid surface (spatial statistics and microstructural descriptors are dealt with in Section 2.5). Materials with similar volume fractions may have different pore size distributions, meaning that some regions have a higher particle density. It would be desirable to

explicitly include a dependence on pore sizes, and hence end up with the following form of the Kozeny-Carman equation:

$$\kappa = \tilde{C}f(\Lambda)\frac{\Phi_{void}^3}{S^2(1 - \Phi_{void})^2}, \quad (2.4)$$

where $C = \tilde{C}f(\Lambda)$ and $f(\Lambda)$ is a function of some property Λ related to the pore size distribution. One suggestion has been to relate the permeability to the square of some characteristic pore size [10]. However, this is a relation still absent in Eq. (2.3). A simplification of the problem is depicted in Fig. 2.1. The solid volume fraction and hence also the porosity and the specific surface are kept constant. Still, the two geometries are quite different, and a difference in pore sizes can be observed. Particles that tend to create clusters may give rise to more open regions in the structures, which is a phenomenon not captured explicitly in Eq. (2.3).

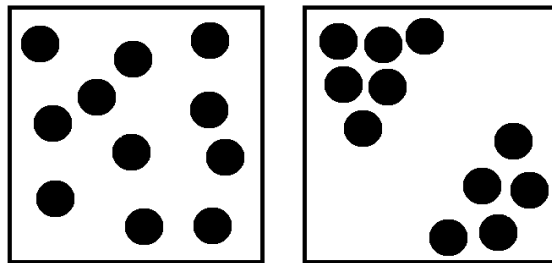


Figure 2.1: Uniformly distributed particles (left) and clustered particles (right).

2.3 Models for granular materials and particle packings

The challenge of packing spherical objects in the most efficient way is an old problem known as the cannonball packing problem [17]. Kepler proposed in the 17th century that the densest packing of identical spheres is obtained by the face-centered cubic pattern (fcc pattern) with a solid volume fraction, or packing fraction, of $\pi/\sqrt{18} \approx 0.74$ [17]. Any proof of Kepler's proposal was, however, lacking, and around three hundred years later, the problem still baffled mathematicians. In 1900, David Hilbert presented a list of 23 unresolved mathematical problems for the time being. Number 18 was concerning the cannonball packing [17, 18]. It took around an additional hundred years until a proof based on computer simulations was obtained, that confirmed Kepler's proposal from four hundred years earlier, i.e. that the maximum packing fraction of identical spheres is around 0.74 [17].

This limit in solid volume fraction is however not restricted to the fcc pattern exclusively. The hexagonal close-packing (hcp pattern), for which the layers are staggered compared to the fcc pattern, gives rise to the same packing fraction as an fcc structure [17]. The layers in an fcc-based structure is repeated for every third layer, whereas in hcp, layers are repeated for every second layer. Both the fcc and the hcp structures are so-called lattice structures, meaning that the particles are arranged in a periodic manner. Other lattice structures are for example the

simple cubic (sc) lattice and the body-centered (bc) lattice. All four examples are cubic systems. There are, however, six other groups of lattices: triclinic, monoclinic, orthorhombic, tetragonal, trigonal and hexagonal lattices [19]. These groups will not be dealt with further in this project. An illustration of the sc, bcc and fcc structures are found in Fig. 2.2.

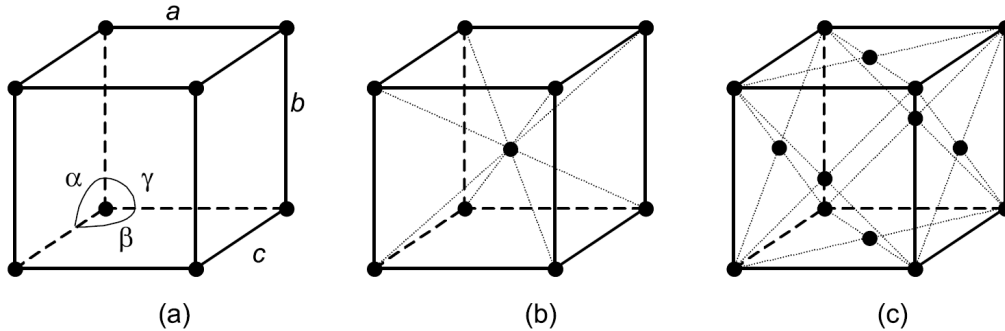


Figure 2.2: Cubic lattices. (a) is simple cubic, (b) is body-centred cubic, and (c) is face-centred cubic. In all cells, $\alpha = \beta = \gamma = \pi/2$ and $a = b = c$. Figure taken from [1].

In addition to the lattice-based structures, there are structures of a more random nature, one class being random close packings (RCP). A precise definition of the RCP state does not exist, since the obtained packing fraction depends on the used (experimental or simulation) protocol, but a description of the state would be structures of randomly distributed particles packed to a maximum possible density [20]. Experiments based on pouring a large number of uniform balls into a vessel, and having them shaken down to stable positions, show that a maximum packing fraction of spherical particles of equal size, i.e. monodisperse spheres, is around 0.637 [21]. The maximum packing fraction of monodisperse spheres depends, however, on the system size. To reach the maximum packing fraction, an infinite system is needed. For a certain system of size h , the expected packing fraction Φ_{RCP} is

$$\Phi_{\text{RCP}} = \Phi_{\text{RCP}}^{\infty} - C/h, \quad (2.5)$$

where C is a fitting constant and $\Phi_{\text{RCP}}^{\infty}$ is the packing fraction as $h \rightarrow \infty$ [22]. Another class of random packings are random-loose packings (RLP), which have densities below the maximum packing fraction [23, 24]. Like the RCP state, the definition of RLP is somewhat vague, but it represents the lowest possible packing fraction still mechanically stable [24].

The particle size distribution affects the maximum packing fraction in RCP [22, 25]. Experiments and simulations show that by introducing a polydisperse size distribution, meaning that particles of different sizes are allowed in the structure, the packing fraction for RCP can reach above the limit for a monodisperse distribution [22]. A denser packing is achieved as smaller particles are filling the void between the larger ones, space otherwise inaccessible. Also, the particle shape has an impact of the maximum packing fraction [25–27]. Simulations show that as the aspect ratio α of the particles changes, the packing fraction reaches a maximum value of around 0.71 ($\alpha \approx 1.5$ (prolate) and $\alpha \approx 0.67$ (oblate)) [27]. As α increases (decreases) for

prolate (oblate) particles, the maximum packing fraction decreases, which may be related to the strong excluded-volume effects in such structures [27].

As a diversity in the particle sizes is introduced, the specific surface of the system may change. Two structures that have the same solid volume fractions may have different specific surfaces. Smaller particles have larger area per unit volume, which affects the total surface area. It can be shown with an example how the specific surface is expected to behave when introducing a polydisperse size distribution and see how the surface area changes. Assume two systems are consisting of only two particles each¹. Let the first system, 1, contain two identical particles with radius r , and the second system, 2, contain two particles with radii $r - a$ and $r + b$ where $a, b \geq 0$ are some constants. In 1, the total surface area of the particles and the total solid volume are

$$\begin{aligned} A_1 &= 8\pi r^2, \\ V_1 &= \frac{8\pi}{3} r^3, \end{aligned} \quad (2.6)$$

and in 2 they are

$$\begin{aligned} A_2 &= 4\pi[(r - a)^2 + (r + b)^2], \\ V_2 &= \frac{4\pi}{3}[(r - a)^3 + (r + b)^3]. \end{aligned} \quad (2.7)$$

Let the solid volumes be equal, yielding that

$$(r + b) = (2r^3 - (r - a)^3)^{1/3}. \quad (2.8)$$

Using the above result, the expression for A_2 can be rewritten accordingly:

$$A_2 = 4\pi \left[(r - a)^2 + (2r^3 - (r - a)^3)^{2/3} \right]. \quad (2.9)$$

Now, the derivative $\frac{\partial A_2}{\partial a}$ is

$$\frac{\partial A_2}{\partial a} = 8\pi \left[-(r - a) + \frac{(r - a)^2}{[2r^3 - (r - a)^3]^{1/3}} \right] \quad (2.10)$$

and setting $\frac{\partial A_2}{\partial a} = 0$ yields the optimum $a = 0$. The nature of this optimum is given by the sign of $\frac{\partial^2 A_2}{\partial a^2}$. Taking the derivative once more,

$$\frac{\partial^2 A_2}{\partial a^2} = 8\pi \left[1 - \frac{2(r - a)}{[2r^3 - (r - a)^3]^{1/3}} - \frac{(r - a)^4}{[2r^3 - (r - a)^3]^{4/3}} \right], \quad (2.11)$$

and inserting $a = 0$ yields $\frac{\partial^2 A_2}{\partial a^2}|_{a=0} = -16\pi < 0$. Hence, the optimum is a maximum, and corresponds to the largest value of the specific surface, and by introducing a variety of particle sizes in the distribution, the area, and in the extent the specific surface, decreases.

¹Note that the example is transferable to a larger system of particles, as long as the number

2.4 Simulation techniques

2.4.1 Techniques for generating virtual material structures

Virtual material structures can be generated by using different approaches, deterministic as well as stochastic, or a combination of the two. Molecular dynamics models are based on simulating particle interactions by Newtonian mechanics, where the force

$$\vec{F}_i = m_i \frac{d^2 \vec{r}_i}{dt^2} \quad (2.12)$$

on a particle i depends on its surrounding and its interactions with the other particles in the domain [3]. In contrast to this deterministic approach, Monte Carlo simulations are based on stochasticity. The idea is to simulate random particle movements and interactions instead of deterministic ones. Most Monte Carlo methods do not include the equations of motion. Such models are suitable for modelling systems where the static, and not the dynamic, properties are of interest. Brownian dynamics methods, on the other hand, include both the equations of motion and stochasticity. A deterministic part, including contributions as external forces and friction, is complemented by a random force [3].

In methods based on sequential deposition of particles, virtual particles are dropped one at a time into a simulated gravitational field, and subsequently settle in the domain. Note that Newton's equations are not solved for the particles as they fall. Instead, particles use rotational and translational motion to achieve the steepest descent on its downward trajectory. A falling particle interacts with the current structure and settles in a stable position corresponding to a minimum potential energy [28]. After settling, the particle positions are fixed. However, some sequential deposition methods have implemented a step where a shaking of the vessel, like in some experimental procedures [21], is simulated [28].

2.4.2 Fluid flow modelling

A common approach in fluid flow modelling is to consider macroscopic properties of the flow, such as velocity, temperature, pressure and density. A successful and often used method, based on this approach, is the finite volume method (FVM). Fundamental parts of FVM are (i) integration over a small control volume δV of the problem-dependent governing equations, and (ii) conservation laws (conservation of mass, Newton's second law and the first law of thermodynamics) [29]. The essential equation in fluid dynamics is the Navier-Stokes equation, which for incompressible flow and constant viscosity μ is given by

$$\rho \frac{dv_i}{dt} = -\frac{\partial p}{\partial x_i} + \mu \sum_j \frac{\partial^2 v_i}{\partial x_j \partial x_j} + \rho f_i, \quad (2.13)$$

where ρ is the density, v_i is the velocity in direction i , p is the pressure and f_i is the body forces in direction i , e.g. gravitational or electromagnetic forces [30]. Equation

fraction of the two kinds are the same (50/50).

(2.13) is a transport equation for momentum in direction i . A convection-diffusion equation for a general variable ϕ is given by

$$\frac{\partial}{\partial t}(\rho\phi) + \nabla \cdot (\rho\phi\vec{u}) = \nabla \cdot (\Gamma\nabla\phi) + S_\phi, \quad (2.14)$$

where \vec{u} is the velocity and Γ is the diffusion coefficient. The terms, from left to right, correspond to a transient term, convection, diffusion and a source term.

Following the FVM principles, Eq. (2.14) is integrated over δV in space and Δt in time, which yields

$$\begin{aligned} \int_{\Delta t} \frac{\partial}{\partial t} \left(\int_{\delta V} (\rho\phi) dV \right) dt + \int_{\Delta t} \int_A \vec{n} \cdot (\rho\phi\vec{u}) dAdt \\ = \int_{\Delta t} \int_A \vec{n} \cdot (\Gamma\nabla\phi) dAdt + \int_{\Delta t} \int_{\delta V} S_\phi dV dt, \end{aligned} \quad (2.15)$$

where Gauss theorem has been used to transform the volume integral of the convective and diffusive terms into surface integrals over the bounding surface A . Equation (2.15) is then discretized using the control volume δV and associated (proper) discretization schemes² and the conservation laws [29]. An illustration of a control volume $\delta V = \Delta x$ in 1-D enclosing a lattice point P in a discretized space is found in Fig. 2.3. The integration interval is $[w, e]$, indicating the west and east faces of the control volume, respectively. For the interested reader, a detailed analysis of FVM is found in [29].

In complex geometries with irregular boundaries, e.g. soft matter and porous media, it may be difficult to set up the boundary conditions needed for simulating the macroscopic flow properties in FVM. In such cases, it is beneficial to use interactions on a mesoscopic scale to describe macroscopic flow properties [31]. One method utilizing this concept is the lattice Boltzmann method (LBM) [3, 31]. LBM originates from the lattice gas cellular automata, which is a simplified description of molecular interactions of a gas, where virtual particles move and interact on a lattice [31]. Instead of considering single particles, LBM employs concepts from statistical mechanics³ and provides a particle distribution function $f(\vec{r}, \vec{v}, t)$ for the lattice sites. The (fluid) particles, which in turn are collections of molecules, translate between lattice sites [3], and from the microscopic states it is possible to obtain macroscopic flow properties, such as density and velocity. A more detailed description of LBM is found in Section 3.2.1.

²Properties such as conservativeness, boundedness and transportiveness differ between schemes. The choice of scheme may depend on the term in question.

³A short introduction to statistical mechanics is found in Appendix A.1.

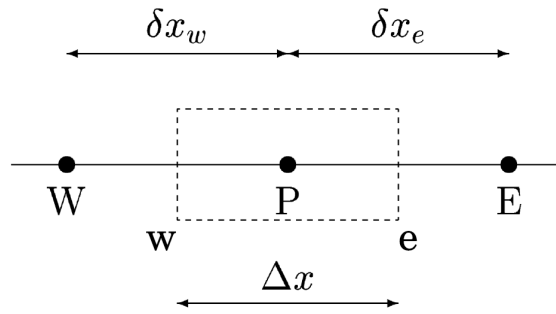


Figure 2.3: Control volume $\delta V = \Delta x$ used in 1-D FVM. Figure taken from [2].

2.5 Spatial statistics

As has been seen in above sections, there is a relationship between microscopic properties of the material and macroscopic properties of the flow. Hence, to facilitate a prediction of the permeability, some sort of characterization of the material through microstructural descriptors would be beneficial, one approach being microstructural correlation functions. There are several microstructural descriptors, e.g. n -point probability functions, surface correlation functions, the lineal-path function, the chord-length density function and the pore size distribution function, to name a few. The n -point probability function and the pore size distribution function will be used later to characterize structures. Hence, these descriptors will be explained below. For further information about other microstructural correlation functions, the reader is referred to [4].

2.5.1 Pore size probability density function

The pore size probability density function $P(\delta)$ for isotropic media is defined as in [4]:

$$P(\delta)d\delta = \text{Probability that a randomly chosen point in a realization of the pore phase lies at a distance between } \delta \text{ and } \delta + d\delta \text{ from the nearest point on the pore-solid interface.} \quad (2.16)$$

Normalization yields

$$\int_0^{\infty} P(\delta)d\delta = 1. \quad (2.17)$$

In three dimensions, the distribution of the pore sizes is equivalent to the distribution of sphere radii [4].

2.5.2 n -point probability function

The n -point probability function is, as well as the pore size probability density function, a measure based on a probabilistic description of the structure. Consider a sample space Ω , where the points $\omega \in \Omega$ constitute a random realization of the medium. If the system considered is consisting of two separate phases (solid and

void), $i = 1, 2$, they will occupy subsets ν_i so that $\nu_1 \cup \nu_2 = \nu$ and $\nu_1 \cap \nu_2 = \emptyset$. Then, for a point at position \vec{x} and for a certain realization ω , an indicator function $\mathcal{I}^{(i)}(\vec{x}; \omega)$ can be defined as

$$\mathcal{I}^{(i)}(\vec{x}; \omega) = \begin{cases} 1 & \text{if } \vec{x} \in \nu_i(\omega) \\ 0 & \text{otherwise} \end{cases} \quad (2.18)$$

Hence,

$$\mathcal{P} \left\{ \mathcal{I}^{(i)}(\vec{x}; \omega) = 1 \right\} + \mathcal{P} \left\{ \mathcal{I}^{(i)}(\vec{x}; \omega) = 0 \right\} = 1. \quad (2.19)$$

The expectation value of $\mathcal{I}^{(i)}(\vec{x}; \omega)$ is given by

$$\begin{aligned} \langle \mathcal{I}^{(i)}(\vec{x}; \omega) \rangle &= \mathcal{P} \left\{ \mathcal{I}^{(i)}(\vec{x}; \omega) = 1 \right\} \cdot 1 + \mathcal{P} \left\{ \mathcal{I}^{(i)}(\vec{x}; \omega) = 0 \right\} \cdot 0 \\ &= \mathcal{P} \left\{ \mathcal{I}^{(i)}(\vec{x}; \omega) = 1 \right\}, \end{aligned} \quad (2.20)$$

and hence, in this case, is the same as the probability of finding a point at position \vec{x} in phase i . Using this result, a one-point probability function $S_1^{(i)}(\vec{x})$ can be defined as

$$\begin{aligned} S_1^{(i)}(\vec{x}) &:= \langle \mathcal{I}^{(i)}(\vec{x}; \omega) \rangle \\ &= \mathcal{P} \left\{ \mathcal{I}^{(i)}(\vec{x}; \omega) = 1 \right\}, \end{aligned} \quad (2.21)$$

which gives the probability of \vec{x} being located in the phase i , an equivalent to the volume fraction.

The case for $n = 2$, the two-point probability function $S_2^{(i)}(\vec{x}_1, \vec{x}_2)$ for a phase i , is also an interesting case. It is defined as

$$\begin{aligned} S_2^{(i)}(\vec{x}_1, \vec{x}_2) &:= \langle \mathcal{I}^{(i)}(\vec{x}_1; \omega) \mathcal{I}^{(i)}(\vec{x}_2; \omega) \rangle \\ &= \mathcal{P} \left\{ \mathcal{I}^{(i)}(\vec{x}_1; \omega) = 1, \mathcal{I}^{(i)}(\vec{x}_2; \omega) = 1 \right\}, \end{aligned} \quad (2.22)$$

and describes the probability of two randomly generated points at positions \vec{x}_1 and \vec{x}_2 to be located in phase i . A further analysis of $S_2^{(i)}(\vec{x}_1, \vec{x}_2)$ is performed in Section 3.3.2.

By following the above reasoning, a generalization for n points may be performed, and the n -point probability function $S_n^{(i)}(\vec{x}_1, \vec{x}_2, \dots, \vec{x}_n)$ is hence defined as

$$\begin{aligned} S_n^{(i)}(\vec{x}_1, \vec{x}_2, \dots, \vec{x}_n) &:= \langle \mathcal{I}^{(i)}(\vec{x}_1; \omega) \mathcal{I}^{(i)}(\vec{x}_2; \omega) \dots \mathcal{I}^{(i)}(\vec{x}_n; \omega) \rangle \\ &= \mathcal{P} \left\{ \mathcal{I}^{(i)}(\vec{x}_1; \omega) = 1, \mathcal{I}^{(i)}(\vec{x}_2; \omega) = 1, \dots, \mathcal{I}^{(i)}(\vec{x}_n; \omega) = 1 \right\}, \end{aligned} \quad (2.23)$$

which is the probability of the n points positioned at $\vec{x}_1, \vec{x}_2, \dots, \vec{x}_n$ are located in phase i [4].

2.6 Related earlier work

Material design and fluid dynamics are already on an individual basis two major fields of research, and combining them generates a vast space of physics to explore. Earlier investigations relating the particle shape to a material's transport properties have been conducted, where packings of ellipsoidal, cylindrical and parallelepipedic grains of identical size were investigated, where an impact of the particle type was observed [28]. The effect of size distribution has been dealt with as well. In one study, the choice of size distribution and related effects on diffusion was investigated, and an analysis of the spatial statistics of the structure was performed [32]. No convective flow was, however, considered, and despite the detailed analysis, a more exhaustive and systematic exploration of the space of material structures would be preferable.

3

Methods

3.1 Generating virtual granular materials

The granular structures were generated using a Monte Carlo-based simulation method. Initially, spherical particles were randomly distributed throughout the domain by picking positions based on a uniform distribution inside simulation domain $[0, L]^3$ for $L = 1$. The initial particle radii were set by specifying an initial volume fraction Φ_0 ,

$$\Phi_0 = \frac{4\pi}{3V} \sum r_i^3, \quad (3.1)$$

to start with. For identical particles, $\sum r_i^3$ simplifies to Nr^3 , where N is the number of particles.

Periodic boundary conditions were used, which means that portions of the particles that happened to be located outside the interval $[0, L]$ in any direction were cut off and moved to enter with corresponding volume on the opposite side of the domain. In other words, for a particle i , its position $\vec{R}_i(x, y, z)$ fulfilled the relation

$$\vec{R}_i \rightarrow \vec{R}_i \pmod{L}. \quad (3.2)$$

A concept similar to energy was introduced. For the particle i at position \vec{R}_i , an energy $E(\vec{R}_i)$ was defined as:

$$E_i(\vec{R}_i) = \sum_{\text{overlapping particles}} 1/R_{i,j}^\alpha \quad (3.3)$$

where $R_{i,j} = |\vec{R}_{i,j}|$ is the distance between the centers of particle i and particle j , and $\alpha > 0$ is a constant. The particles were forced to find positions with successively lower (or equally high/low) energy until $E_i(\vec{R}_i) = 0$, i.e. no overlap occurred, for all i . In one sweep, i.e. in a loop over all particles, a small displacement $\Delta\vec{R}_i$ was randomly drawn from a normal distribution for each particle. A corresponding energy $E_{i,new}$ for the new particle position $\vec{R}_{i,new} = \vec{R}_i + \Delta\vec{R}_i$ was calculated. If $E_{i,new} \leq E_{i,old}$, the position for particle i was updated to the new position. Otherwise, its old position was kept. Also free particles (with an energy $E = 0$) were allowed to move, even though they had no energy, as long as the new position did not lead to an increase in energy. Considering also the nonoverlapping particles, allowing them to move too, were helping overlapping particles to find better positions by opening up regions in the domain otherwise blocked by fixed free particles.

It is advantageous to keep track of the frequency of accepted displacements $\Delta\vec{R}_i$ and to control the magnitude of $\Delta\vec{R}_i$, especially as the material is getting denser.

Keeping the displacements very small yields a high acceptance rate, since the chance of finding a position with lower energy is high. However, such a method would become very inefficient, since a large number of sweeps would be necessary to get the overlaps resolved. Too large magnitudes of $\Delta\vec{R}_i$ risk to almost never be accepted, since the new positions easily could give rise to an even larger overlap with other particles. Hence, controlling the magnitude of the displacement by a factor, which depends on the number of accepted new positions in the previous sweep, scales the displacement to an appropriate value suitable for the current volume fraction. This type of scaling was implemented in the simulation for all methods involving particle displacements introduced below, i.e. the magnitude of the corrections was controlled in such way so that the rate of accepted displacements was kept within the interval $]0.25, 0.40[$, where the magnitude of the scaling was decreased or increased for too low or too high acceptance rate, respectively.

The algorithm continued until no particle overlap occurred. When the condition of no overlap was fulfilled for a specific solid volume fraction Φ_i , the particle radii were increased so that the solid volume fraction increased with some constant ϵ , i.e.

$$\Phi_{i+1} = \Phi_i + \epsilon \quad (3.4)$$

where ϵ typically in the range $10^{-5} - 10^{-4}$. As shrinking the domain and letting the radii expand are equivalent, a relation for the corresponding radii in step $i + 1$ was achieved by realizing that $\Phi_{i+1} = C_i\Phi_i$ where C_i is a factor specific for the iteration step i . Using this yields

$$\Phi_i + \epsilon = C_i\Phi_i \quad \implies \quad C_i = \frac{\Phi_i + \epsilon}{\Phi_i}. \quad (3.5)$$

Since $\Phi \sim r^3$, the equation for r_{i+1} is given by

$$\begin{aligned} r_{i+1} &= C_i^{1/3} r_i \\ &= \left(\frac{\Phi_i + \epsilon}{\Phi_i} \right)^{1/3} r_i, \end{aligned} \quad (3.6)$$

which was used in the simulations in order to update the volume fractions of the solid phase.

The computational time needed for the simulations depended on the number of particles. Consideration was taken to computational time and physical relevance of the system, and a number of 250 particles was used unless otherwise stated.

3.1.1 Polydisperse size distribution

Some additional steps were done in the cases of polydisperse size distributions, which were created in two steps. A set of radii was selected, without concern to the solid volume fraction. Hence, the radii had to be scaled so that the particle volumes would add up to the correct starting volume fraction. From the original volume

fraction Φ_{org} of a structure,

$$\Phi_{org} = \frac{4\pi}{3V} \sum r_{i,org}^3, \quad (3.7)$$

where $\{r_{i,org}\}$ is the set of original radii, and the desired starting volume fraction Φ_0 , a correction for the radii was calculated. Since $\Phi \sim r^3$, the correct starting radius r_i for particle i was

$$r_i = \left(\frac{\Phi_0}{\Phi_{org}} \right)^{1/3} r_{i,org}. \quad (3.8)$$

Two cases of polydisperse size distributions were investigated, the lognormal distribution with parameters μ and σ (corresponding to the exponent of a normal distribution with mean μ and standard deviation σ), whose logarithm is normally distributed, and the bidisperse distribution, which consists of only two different particle sizes. The scaling of the radii was performed as described above. Since only relative values were of interest, no comparison to experimental results was done, this type of scaling works. The coefficient of variation δ , though,

$$\delta = \frac{\sigma(r)}{\bar{r}} \quad (3.9)$$

was constant throughout a series as the particles were expanding. For the bidisperse distribution, the varied parameters were the size ratio between the particles and the number of small/large particles.

3.1.2 Lattice structures and random packings

An interesting class of materials are the so-called semicrystalline, which contain regions of both crystal structure and random regions. An emerging problem, though, is that it is not possible to obtain packing fractions above around 0.64 for RCP¹. Hence, the process described in Section 3.1 was not applicable. A way to overcome the problem was to employ a "reversed" process, meaning that instead of compressing the domain (letting the particles expand) until a desired packing fraction was reached, the implemented process started from an fcc lattice structure, which possesses the largest possible packing fraction for a monodisperse size distribution. The domain was then decompressed (the particles were compressed) successively to generate a set of desired solid volume fractions, ranging in *reversed* order, i.e. from $\Phi_{max} = \pi/\sqrt{18} = 0.7403$ to some Φ_{min} . In order to introduce random features in the structures, the particles, after successively expanding the domain, were allowed to move for a number of sweeps. Displacements ΔR for a particle i was randomly generated, and an energy $E_{i,new}$ was calculated using Eq. (3.3). The original interaction energy for every particle was $E = 0$, since the starting positions were corresponding to the lattice positions, and if $E_{i,new} = 0$, meaning no new overlaps were created in the process, the new position was kept. If, however, any overlaps were created, the old position was kept. This procedure will from hereon be referred to as the lattice method.

¹The chance of obtaining packing fractions above around 0.64 for RCP is vanishingly small,

3.1.3 Modifying the structure

As mentioned in Section 2.2, there is no explicit dependence on the pore size distribution in the Kozeny-Carman equation, and some geometric properties are hidden in the constant C . It would be desirable to have some sort of control over the pore sizes, and in turn investigate the link between geometric properties of the structures and the permeability. A way to proceed in this investigation was to modify structures after $E = 0$ was reached, in that sense that the particles were relocated compared to the original structures. Hence, the pore size distribution was changed while keeping the specific surface and porosity constant. To that end, different methods for controlling the spatial distribution of the particles were implemented: (i) a purely attractive force was introduced between the particles to make them create clusters, (ii) a potential inspired by the Lennard-Jones potential, consisting of both an attractive and a repulsive force between the particles was introduced, (iii) a bidisperse distribution of particles, for which the larger particles were deleted after unraveling overlapping particles, was generated and (iv) repulsive point potentials were introduced in the domain, already in the generating process, in order to push the particles together.

3.1.3.1 Attractive force between particles

The method used to achieve an attractive force between the particles was similar to the way the overlaps were resolved. A sweep over all particles was performed, and for every particle i , an energy E_i was calculated:

$$\begin{aligned} E_i &= \sum_{\text{all particles } j \neq i} \frac{1}{\left[R_{i,j} - (r_i^* + r_j^*) \right]^\alpha} \\ &= \sum_{\text{all particles } j \neq i} E_j^{(i)} \end{aligned} \quad (3.10)$$

Here, $R_{i,j}$ is the distance between the centers of particles i and j , $\alpha > 0$ is some odd integer, r_i^* and r_j^* are the particle radii of particle i and j , respectively, and $E_j^{(i)}$ is the energy contribution of particle j to E_i . As can be seen, $E_j^{(i)} \rightarrow \infty$ as the particle surfaces meet. If the particles are overlapping, the energy contribution is negative. A small displacement $\Delta \vec{R}$ was drawn randomly from a normal distribution, and a new corresponding energy $E_{i,new}$ was calculated. If the condition $E_{i,new} \geq E_{i,old}$, where $E_{i,old}$ corresponds to the former energy, held, and if no energy contributions were negative (i.e. no overlaps were created), the particle position was updated. Otherwise, the old position was kept. As seen, the negative sign of the energy contribution of overlapping particles facilitates the monitoring of forbidden updates of the positions corresponding to creation of overlaps (unaccepted displacements). If α were to attain an even value, it would not be possible to distinguish between overlapping and nonoverlapping positions in Eq. (3.10), since the square of the denominator, and hence the energy contribution, would be positive for both the overlapping and nonoverlapping positions. Since there is no clear goal for the

and hence considered practically impossible.

algorithm to reach, like in the case of packing the particles to a certain volume fraction, a limit of maximum number of sweeps was set. Different approaches can be employed in order to find an appropriate number of sweeps. For this method, the mean pore size was monitored in a trial run, and the number of sweeps needed until the change between sweeps was negligible was estimated. Another possible quantity to monitor is the interaction energy between the particles, which should decrease as a function of sweeps. Monitoring particle interaction energy might, however, be a more reliable approach compared to monitoring the mean pore sizes, and was hence the preferred approach in other methods described below.

3.1.3.2 Attractive and repulsive forces between particles

A potential inspired by the Lennard-Jones potential was introduced, including both an attractive and a repulsive part in the interaction energy between particles. The method is in principle the same as the one described in Section 3.1.3.1, where only an attractive force was considered. For a particle i , an interaction energy E_i is defined accordingly:

$$\begin{aligned}
 E_i &= \sum_{\text{all particles } j \neq i} \left(\frac{1}{[R_{i,j} - (r_i^* + r_j^*)]^\alpha} - \frac{1}{[R_{i,j} - (r_i^* + r_j^*)]^\beta} \right) \\
 &= \sum_{\text{all particles } j \neq i} E_j^{(i)}.
 \end{aligned} \tag{3.11}$$

where $\alpha > \beta > 0$ are some integers. To facilitate the monitoring of overlapping particles, α is odd. The choice of β (odd or even) does not really matter, since the first term on the LHS in Eq. (3.11) will dominate (for $\alpha > \beta > 0$) in the overlapping region. The procedure regarding the update of particle positions was identical to the former case.

3.1.3.3 Introducing repulsive point potentials in the domain

Another way to force particles together is to introduce randomly distributed points in the domain working as repulsive potentials, pushing the particles away from certain regions. For a particle i , the energy E_i corresponding to the interaction with N potentials is defined as

$$E_i = \sum_{j=1}^N \frac{1}{R_j^\alpha} \tag{3.12}$$

where R_j is the distance between the center of particle i and potential j and $\alpha > 0$ is some integer. A high energy was considered disadvantageous, and hence the particles were forced to find positions minimizing the energy. A new position was evaluated, and if the the energy decreased under the constraint that no overlaps were created the new particle position was kept. Trial runs were performed in order to find out the number of sweeps needed to find an energy minimum in the system (i.e. minimizing the energy for all particles). For every sweep, the total energy was calculated, and when the energy stabilized, i.e. was approximately constant for a certain number of sweeps, the system was considered to be in equilibrium.

3.1.3.4 Selectively deleting one type of particle in structures

The idea of the model is to generate structures based on bidisperse size distributions. After successfully having all the overlaps resolved, the larger particles were deleted from the structures. Hence, pore sizes of at least the size of the deleted particles would be produced. This method is of interest due to possible industrial applications, where materials are constructed using two types of particles. In a second stage, one of the particle types is removed from the structures using e.g. heat or a chemical procedure, leaving pores of the size of the deleted particles. Since there exists an interest in translating the theoretical approach in this method to an actual production of physical materials, the physical relevance in the setup of the algorithm was crucial. Hence, the size of the remaining smaller particles was kept constant, and an increase of the solid volume fraction was achieved by increasing the number of particles (instead of changing the size of the particles). A similar approach was implemented for the larger particles (which were to be deleted in the second stage).

3.1.4 Triangulating the surface using VoxSurface

Before investigating material properties in Gesualdo, generated structures need to be converted to triangulated surfaces. A discretization was performed in Matlab generating $N \times N \times N$ binary structures, for $N = 300$, where 0 corresponded to a voxel position occupied by void and 1 corresponded to a voxel position occupied by solid. The structures were exported to multipage `.tif` format and then imported in VoxSurface, a part of the Gesualdo program, where the structures were triangulated. The structures were coarsened and Gaussian smoothing was applied. Also, the resulting structures were prepared for periodic boundary conditions in the upcoming flow simulations. An example of a triangulated structure is found in in Fig. 3.1a.

In the discretization step, involving both the voxelization in Matlab and the triangulation in VoxSurface, the structures were coarsened. The volume fraction changed somewhat, and hence the structures used in the flow simulation were not completely identical to the one originally generated in Matlab. In the example in Fig. 3.1, the initial volume fraction was 0.50 of the total volume. In the triangulated structure, the solid volume fraction was 0.493.

When the discretization step is larger than the distance between the particles, it is not possible to make a distinction between the two surfaces. What happens is that the surfaces tend to get "welded" together, and the particles get connected. This affects both the volume and the surface of the particles, and hence affects the results in the computation of the permeability. An example of welded particles is found in Fig. 3.1b.

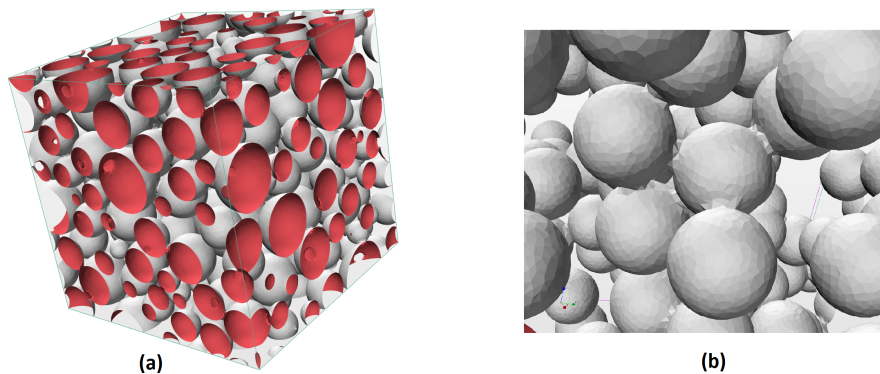


Figure 3.1: (a) An example of a generated structure after triangulation, coarsening and smoothing. The solid volume fraction is around 0.50 (0.493). As can be seen, portions of the particles that are located outside of the domain are cut off and moved to the corresponding opposite side of the volume. (b) Particles close to each other tend to get welded together in the discretization process.

3.2 Mass transport simulations

3.2.1 The lattice Boltzmann method

As mentioned in Section 2.4.2, the lattice Boltzmann method (LBM) utilizes interactions between virtual fluid particles on a mesoscopic scale to describe macroscopic properties of the flow [3, 31]. Instead of considering single particles, a particle distribution function $f(\vec{r}, \vec{v}, t)$ is employed. It is assumed that all particles have the same mass m . Integration of $f(\vec{r}, \vec{v}, t)$ over a velocity interval $\Delta\vec{v}$ gives the number density of particles, i.e. the number of particles per unit volume, within that interval. Hence, the following relations for the macroscopic properties are obtained [31]:

$$\begin{aligned}\rho &= m \int f(\vec{r}, \vec{v}, t) d\vec{v} \\ \rho u_i &= m \int f(\vec{r}, \vec{v}, t) v_i d\vec{v}\end{aligned}\tag{3.13}$$

where ρ is the density of the fluid and u_i is the mean flow velocity in direction i .

As an example, a discrete lattice space is considered, where only transitions between neighboring sites are permitted [3]. A part of a larger two dimensional lattice is found in Fig. 3.2. Assume that particles at time t are positioned at the site in the center of the square (the dot). At time $t + \Delta t$, where Δt is the time step used in the simulation, the possible choices for the particles are to either move to the surrounding sites or to stay in the center. If the distance between neighboring sites in the vertical and horizontal direction is Δx , the velocity for a movement between the center and the sites marked with a star is $v_* = \Delta x / \Delta t$. The velocity for a movement between the center and the corner sites, the sites marked with circles, is then $v_\circ = \sqrt{2}\Delta x / \Delta t = \sqrt{2}v_*$. [3]

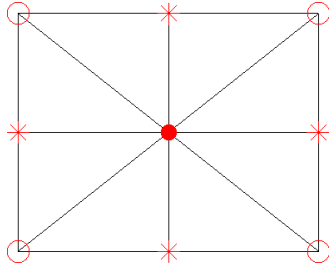


Figure 3.2: A two dimensional example of adjacent lattice sites. Example taken from [3]

A new definition of the particle distribution function may be introduced that incorporates the velocity interval. This definition is suitable for a discrete space. Let $f(\vec{r}, \vec{v}, t) \rightarrow f_\alpha(\vec{r}, t)$, where α corresponds to the direction of the particles with a mean velocity v_α . In the example in Fig. 3.2, $\alpha = \{1, 2, \dots, 9\}$, corresponding to the nine possible transitions between the sites, including staying at the same site, and the mean velocities are 0, v_* and v_o depending on the choice of direction. A summation over all possible directions yields the macroscopic density at a position \vec{r} at time t :

$$m \sum_{\alpha} f_{\alpha}(\vec{r}, t) = \rho(\vec{r}, t). \quad (3.14)$$

Multiplying $f_{\alpha}(\vec{r}, t)$ with the corresponding velocity in the α -direction, followed by a summation over all the directions yields

$$m \sum_{\alpha} f_{\alpha}(\vec{r}, t) v_{\alpha} = \rho(\vec{r}, t) \vec{v}_{mean}, \quad (3.15)$$

where \vec{v}_{mean} is the mean velocity of the flow (the macroscopic flow velocity). Hence, Eq. (3.15) is the momentum of the mean flow per unit volume at the position \vec{r} . From above calculations, it is clear that the macroscopic properties of the flow can be obtained by considering the interactions on a mesoscopic level. [3]

3.2.2 Fluid dynamics simulations

For fluid dynamics simulations, the lattice Boltzmann software tool Gesualdo [33] was used, based on the open-source lattice Boltzmann code Palabos². Gesualdo is developed at the Department of Mathematical Sciences, Chalmers, and an outcome of the VINN Excellence Center SuMo Biomaterials³. With the settings used in Gesualdo for this project, the Navier-Stokes equations are solved for a pressure-driven flow with constant pressure difference across the domain and a no-slip condition on the solid surface [6]. The permeability is calculated using Darcy's law, Eq. (2.2). Since Darcy's law is only valid for laminar flow with small Reynolds number, the pressure gradient driving the flow needs to be small.

The structures generated in VoxSurface were imported in Gesualdo. In order to speed up the calculation, one third of the 300 voxels in all directions was used, i.e.

²www.palabos.org

³www.chalmers.se/en/centres/sumo

the computational grid size was $100 \times 100 \times 100$. Periodic boundary conditions were used for the domain boundaries in all three directions. The convergence tolerance was set to 10^{-4} over 500 iterations. The kinematic viscosity of the fluid was set to $1.004 \cdot 10^{-6}$, i.e. water at 20°C . The resulting force from the pressure gradient was set to 10^{-8} .

3.3 Data analysis and spatial statistics

3.3.1 Calculating pore size distribution

The Matlab function `bwdist` [34] was used to find out the Euclidian distance in units of voxels to the nearest occupied (solid) position. This distance is the maximum possible sphere radius for a particle positioned in that voxel, and hence works as a discrete version of the pore size distribution obtained from the pore size probability density function introduced in Section 2.5.1. A matrix with the same size as the structure, i.e. $N \times N \times N$, containing the maximum possible sphere radii was the result.

3.3.2 Two-point probability function

As mentioned in Section 2.5.2, an interesting case of the n -point probability function is for $n = 2$, $S_2^{(i)}(\vec{x}_1, \vec{x}_2)$. It corresponds to the probability of finding a pair of random points at locations \vec{x}_1 and \vec{x}_2 , separated by a distance $r = |\vec{x}_1 - \vec{x}_2|$, in a certain phase i . For isotropic media, $S_2^{(i)}(\vec{x}_1, \vec{x}_2)$ is not depending on the orientation of the random points, only the separation r . Hence, $S_2^{(i)}(\vec{x}_1, \vec{x}_2) = S_2^{(i)}(r)$. The generated structures are assumed to be isotropic, and hence $S_2^{(i)}(r)$ is used. The argument is dropped from hereon.

The two extreme point separations, $r = 0$ and $r \rightarrow \infty$, correspond to $S_2^{(i)} = \Phi_i$ and $(\Phi_i)^2$, respectively. The behavior of $S_2^{(i)}$ between the two extreme point separations depends on the structure, which is explained by using an example. Two different systems, nonoverlapping and overlapping disks, where the fractions of the phases 1 and 2 are $\Phi^{(1)} = \Phi^{(2)} = 0.5$, are shown in Fig. 3.3. For the nonoverlapping disks, $S_2^{(i)}$ attains its maximum value, corresponding to the fraction of phase i in the system, when $r = 0$. As the separation increases, $S_2^{(i)}$ decays and attains its minimum value for a separation around one disk diameter, to then experience oscillations with a period approximately equal to the disk diameter. This behavior is an effect of the hard-core potential of the disk, where no overlaps are allowed. The asymptotic value is $(\Phi^{(i)})^2 = 0.25$ [4].

Also, for the overlapping disks, the maximum value of $S_2^{(i)}$ is the fraction of phase i , which occurs at $r = 0$. As the separation increases, $S_2^{(i)}$ decays. However, in the case of overlapping disks, there is no minimum at a separation of one disk diameter, and no oscillations occur as the separation increases. Instead, $S_2^{(i)}$ decays to the asymptotic value of $(\Phi^{(i)})^2 = 0.25$ at a separation of one disk diameter, and stays constant. Hence, there is a relation between correlation lengths and oscillations, or dips at certain separation lengths, of S_2 , and the oscillations may be used as an

indicator of the microstructural correlations [4].

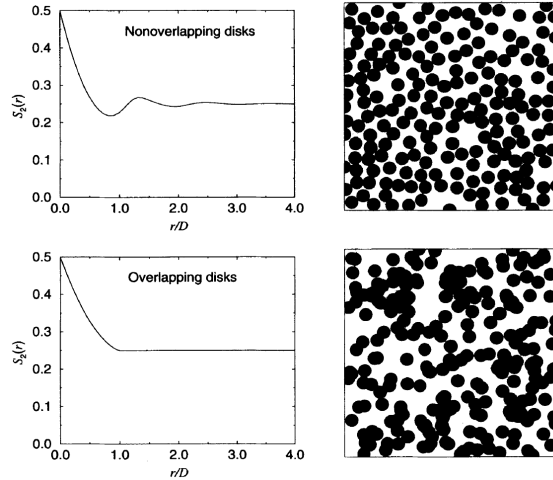


Figure 3.3: Example of two systems, nonoverlapping disks (upper) and overlapping disks (lower). The fractions of the two phases (disk and void) is 0.5. The disk diameter is D and the separation between the end points is r . The example is taken from [4].

The $S_2^{(i)}$ function was implemented and used in the spatial analysis of the structures. A random point located at \vec{x}_1 and a random normalized orientation \hat{r} were picked. For a set of separations

$$\begin{aligned} \Omega &= \{0, r_1, r_2, \dots, r_i, \dots, r_n\} \\ &= d\{0, 1, 2, \dots, i, \dots, n\}, \end{aligned} \quad (3.16)$$

a set of $n + 1$ corresponding points was calculated. Hence, for separation r_i the corresponding point is

$$\vec{x}_2 = r_i \hat{r} = di \hat{r} \quad (3.17)$$

Put simple, the procedure generated a set of points separated by a distance d on a straight line of length dn starting in \vec{x}_1 in direction \hat{r} . If a pair of points \vec{x}_1 and \vec{x}_2 were located in a certain phase i , this was logged as 1, otherwise 0. The procedure was repeated for a (large) number of random \vec{x}_1 and \hat{r} and the set Ω , i.e. a (large) number of straight lines of length dn divided into n sections pointing in arbitrary directions. The probability of finding the pair of points \vec{x}_1 and \vec{x}_2 in phase i as function of the point separation was evaluated and corresponds to $S_2^{(i)}$.

3.3.3 Representation of the results

When generating structures as those presented above, different approaches can be used. For convenience, the algorithms were implemented such that the radii of the particles were increased, instead of shrinking the simulation domain, i.e. the virtual box containing the particles. Both approaches can produce series where the solid volume fraction increases. Important, though, is the representation of the result, and the choice of units. The unit of permeability in the Gesualdo output is voxels².

However, changing the particle sizes, as well as changing the size of the surrounding domain, changes the length scale of the system. Hence, also the physical size of the voxels, and hence the results, are affected. To overcome this issue, the results need to be scaled in some appropriate way by finding a proper length scale. Using the computational resolution set in Gesualdo, a new permeability can be defined as

$$\begin{aligned}\kappa_{physical} &= \frac{\kappa_{simulated}}{\left(\frac{l^2 n^2}{L^2}\right)} \\ &= \frac{\kappa_{simulated}}{f_c}\end{aligned}\tag{3.18}$$

which will have units of some proper length l^2 related to the particle sizes, e.g. the mean radius in the distribution or some other length representative of the particle system. Here, n is the computational resolution in one dimension and L is the length of the side of the cubic domain. The conversion factor, or scale factor is

$$f_c = \frac{l^2 n^2}{L^2}.\tag{3.19}$$

The computational resolution was set to $n = 100$. Note that n specifies the computational grid size in Gesualdo, i.e. the number of grid points actually used in the fluid dynamics simulation, and must not be mistaken for the number of voxels used in the discretization of the structures in Matlab.

Quantities θ in units of length (in contrast to length²), such as the pore sizes, scales in a similar way, namely

$$\theta_{physical} = \frac{\theta_{simulated}}{\sqrt{f_c}}.\tag{3.20}$$

The resulting quantity will have the unit l .

The Gesualdo output contains the total area of the solid in units of voxels, which can be converted to specific surface in units of l^{-1} using the total number of voxels in the domain. The specific surface S is given by

$$S = \frac{n_{surface}}{n^3} \sqrt{f_c},\tag{3.21}$$

where $n_{surface}$ is the total area of the solid in units of voxels.

3.4 Simulation setup

Four major cases were dealt with. In Chapter 4 they are named accordingly: (i) Comparison of size distributions, (ii) The bidisperse size distribution, (iii) From lattice structures to random packings and (iv) Investigations of effects related to spatial correlations. The specific setups and parameter settings are presented here.

3.4.1 Comparison of size distributions

Three series of structures with volume fractions ranging from 0.30 to 0.63 were generated. The first series consisted of identical particles, and in the two other,

different particle radii were used. One was based on a lognormal size distribution and the other was based on a bidisperse size distribution. The lognormal distribution was generated in two steps as explained in Section 3.1.1. First, a set of radii was picked from a lognormal distribution with $\mu = 1$ and $\sigma = 0.3$, then the radii were scaled to get the correct starting volume fraction. For the bidisperse distribution, the size ratio between the particles was 0.5 and the number fraction of small particles was 0.4. A histogram of the scaled radii (so that $r \in [0, 1]$) in the lognormal case is found in Fig. 3.4 below. The coefficient of variation is $\delta = 0.2744$. Since the number of particles is still quite low (250), a higher value of δ sometimes generated single particles having very large radii compared to the smaller ones. This was considered an extreme case, and was not desired. Hence, δ was kept around 0.3.

The compression of the systems continued until a maximum packing fraction was reached, which was considered to have occurred when a maximum number of sweeps, where in every sweep the overlapping particles were trying to find better positions for a certain volume fraction $\Phi_{new} = \Phi_{old} + \Delta\Phi$, was reached. If some particles still overlapped after reaching the maximum number of sweeps, the last accepted structure (without overlap) was considered to possess the maximum packing fraction for the distribution in question. In these cases, the maximum number of sweeps was around 4,000.

The scale factor Eq. (3.19) was based on

$$l = \left(\frac{1}{N} \sum_{i=1}^N r_i^3 \right)^{(1/3)}, \quad (3.22)$$

which is the same for all three distributions for a specific volume fraction (since all three have the same solid volume fractions), and $L = 1$.

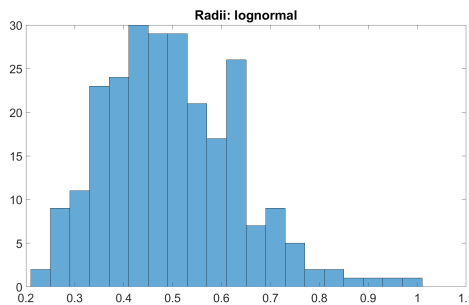


Figure 3.4: A histogram of the scaled radii from the lognormal distribution. The volume fractions are scale independent, and the plot should merely function as a tool to display the spread in the distribution.

3.4.2 The bidisperse size distribution

A series based on bidisperse size distributions was generated, where the fraction of small particles and the size ratio between the larger and smaller particles were varied. The number fraction was varied between 0 and 1, and the size ratio between 0.1 and 1. The total solid volume fraction was held constant and set to 0.50 for all structures.

An appropriate scaling in this case was based on assuming a constant size of the smallest particle throughout the series. Hence, the size of the virtual box containing the particles and the larger particle size had to be changed, in order to fulfill a constant solid volume fraction of 0.50. The smallest of the two particle radii in the distributions was set to 1, and the system and the results were scaled based on this, using Eq. (3.19) with

$$l = r_{small}^{new} = 1; \quad L_{new} = L_{old} \cdot 1/r_{small}^{old}. \quad (3.23)$$

3.4.3 From lattice structures to random packings

A series of structures was generated, with volume fractions going from the maximum possible packing fraction $\pi/\sqrt{18} \approx 0.74$, discussed in Section 2.3, to 0.63. In every step the particles started in the fcc lattice positions. The particle radii were decreased in order for the particles to fill a certain total solid volume fraction. The number of sweeps, for which the particles were allowed to move, was 30,000 for every structure. The scaling procedure was the same as described in Section 3.4.1.

3.4.4 Investigations of effects related to spatial correlations

The scaling procedure was the same as described in Section 3.4.1 for all three cases below.

Introducing forces between the particles

A series of structures with solid volume fractions ranging between 0.2 and 0.4 was generated and then modified afterwards in two different ways. In the first case, an attractive force between particles was introduced, and in the second, both an attractive and a repulsive force were introduced. In both cases, the modification was set to run for 30,000 sweeps for every structure.

Repulsive point potentials

A series of structures, for which the solid volume fraction and the number of repulsive potentials were varied, was generated. The solid volume fraction ranged between 0.2 and 0.4, and the number of repulsive potentials ranged from 0 to 50. The modification was set to run for 500 sweeps.

Deleting particles from the structure

The method was implemented for a fixed number of small particles of a certain size, only changing the number of larger particles which were deleted in a second stage. The number of small particles were 200, which corresponded to a volume fraction of 0.20. The size, as well as the volume fraction, of the larger particles were varied. A choice was made to increase the volume fraction of the larger particles by adding new particles to the system. Hence, the volume fraction of the larger particles increased in steps of particles added. The size of the larger particles was depending of the size ratio.

4

Results and discussion

4.1 Comparison of size distributions

Three sets of structures were generated based on monodisperse, lognormal, and bidisperse size distributions. Comparisons of the permeability and the specific surface are plotted in Fig. 4.1. As can be seen, for lower solid volume fractions, the permeability is higher for the polydisperse size distributions compared to the monodisperse case. Also, the specific surface is smaller in these two cases, a result which corresponds to the theoretical investigation in Section 2.3. There is a resemblance between the bidisperse and the lognormal cases, both regarding permeability and the specific surface. A reason for this might be that in the two polydisperse distributions, particles of both smaller and larger sizes compared to the monodisperse case are allowed (increasing the specific surface of both in comparison to the monodisperse case). With the given distributions, it may be possible that the set of particle sizes introduced in the lognormal distribution, compared to the two sizes in the bidisperse case, does not introduce any significant difference in the packing results. Smaller particles fill the voids between the larger ones in both the bidisperse and the lognormal case, and different packings are hence enabled compared to the monodisperse case. The flattening out of the specific surface observed in the monodisperse case for higher solid volume fractions may be a result of the welding artifact of neighbouring particles described in Section 3.1.4. As the system is compressed, the distances between the particles decrease and the risk for a separation smaller than the discretization step increases. Hence, the risk for welding increases as well. The reason for a less significant effect for the polydisperse distributions may be because of the smaller particles existing in these distributions, which may give rise to configurations inaccessible in the monodisperse case.

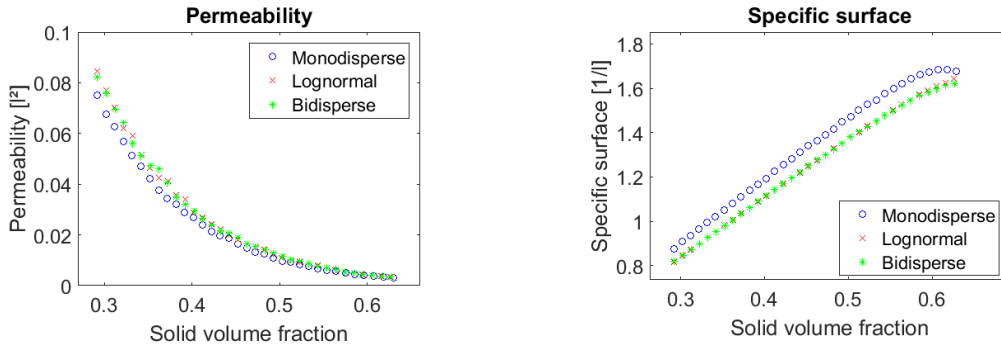


Figure 4.1: Permeability (left) and specific surface (right) for the monodisperse, lognormal and bidisperse size distributions as functions of the solid volume fraction. Note that l is the problem-dependent proper length (see Sections 3.3.3 and 3.4.1).

For all cases, the pore size distributions were calculated and the resulting mean pore sizes are plotted in Fig. 4.2. As can be seen, the mean pore size is slightly larger for the polydisperse cases. Again, the lognormal and the bidisperse distributions virtually coincide. It seems like the additional possible particle configurations give rise to an increase in mean pore size in the polydisperse cases. A comparison between Fig. 4.1 and Fig. 4.2 suggests that there is a relation between an increased mean pore size and an increase of the permeability. Such a relation seems reasonable. The void regions are all connected to one another, and hence establish a network throughout the structures where all pores contribute in the transport process. A larger mean pore size would hence imply a greater possibility for the fluid to pass through.

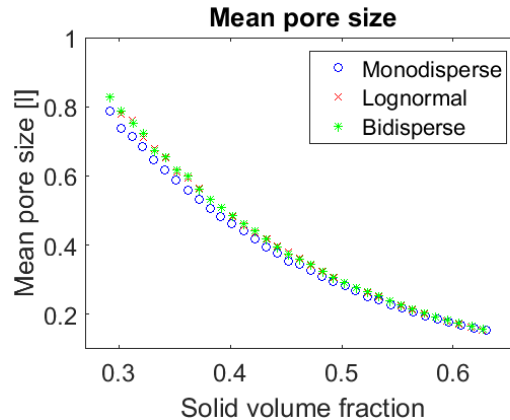


Figure 4.2: Mean pore sizes for the monodisperse, lognormal and bidisperse size distributions as functions of the solid volume fraction. Note that l is the problem-dependent proper length (see Sections 3.3.3 and 3.4.1).

A further investigation shows that there is a linear relation between the square of the mean pore size and the permeability. This assumption holds for all three cases. Plots of comparisons between the squared mean pore size and the permeability are found in Fig. 4.3. The squared mean pore size is scaled with a factor based on minimizing the sum of squared differences to the permeability.

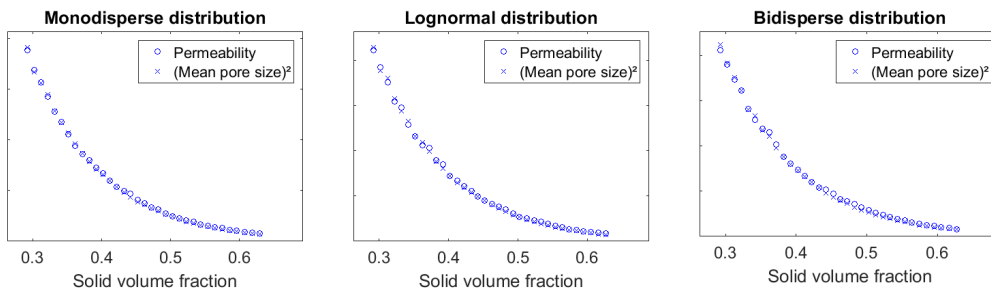


Figure 4.3: Comparison between permeability and squared mean pore size for monodisperse, lognormal and bidisperse distributions as function of the solid volume fraction.

The compression of the systems continued until a maximum packing fraction was reached, and the resulting volume fractions are found in Table 4.1 below. As can be seen, the particle size distribution affects the maximum possible packing fraction, where the largest maximum packing fraction was obtained using a lognormal size distribution, and the smallest was obtained in the monodisperse case. In between is the bidisperse distribution, although this result is dependent upon the parameters of the distributions. Following the reasoning above, smaller particles in the polydisperse cases fill out the void parts between the larger particles. By introducing a set of particle sizes, as in the lognormal case, the number of degrees of freedom increases, and hence a denser packing compared to the bidisperse case is possible. The minimum and maximum values in the lognormal and the bidisperse distributions, scaled with the monodisperse radius, are given by

$$r_{\text{lognormal}} \in [0.3933, 1.8679]; \quad r_{\text{bidisperse}} \in [0.5772, 1.1544]. \quad (4.1)$$

Hence, the spread in the lognormal case is wider, which also might have an effect on the maximum packing fraction. Increasing the size difference in the bidisperse distribution would possibly increase the maximum packing fraction. However, the bidisperse distribution still lacks the vast packing possibilities associated with the set of sizes in the lognormal distribution. What can be concluded, though, is that the maximum packing fraction is affected by introducing a polydisperse size distribution.

An important note is that the packing fractions obtained here were limited by a maximum number of sweeps. It would perhaps be possible to make the structures slightly denser by decreasing $\Delta\Phi$ and increasing the maximum number of sweeps. Also, the number of particles, and equivalently the size of the domain, is limited, which is probably the most important reason for not obtaining denser packings. As mentioned in Section 2.3, the true maximum packing fraction is obtained by letting the domain size go to infinity. Since the particle sizes are scaled with regard to a fixed domain size in such a way that the total particle volume adds up to a desired volume fraction, increasing the domain volume would correspond to increasing the number of particles in the simulation. Due to the computational time, the number of particles needed to be restricted to a convenient number, in these cases set to 250. If more time were at hand it would be possible to increase the number of particles. This increase would then hopefully enable compressing the system to such extent

that a packing fraction of around 0.64 would be obtained for the monodisperse distribution.

Table 4.1: Maximum packing fractions.

Monodisperse	Lognormal	Bidisperse
0.6310	0.6609	0.6512

4.2 The bidisperse size distribution

The resulting permeability for a series of bidisperse size distributions, where the size ratio between the smaller and larger particles and the number fraction of small particles were varied, is plotted in Fig. 4.4. Plots of the mean pore size as a function of the number fraction of small particles for all size ratios are found in Fig. 4.5. A comparison between the permeability and the mean pore size confirms the conclusion in Section 4.1, i.e. that larger average pores seem to imply an increased permeability. When the size ratio is small, i.e. when there is a large difference in size between the two particle types, the permeability stays quite unaffected as larger particles are replaced by smaller ones. However, when the larger particles tend to be quite few, drastic effects for every step in number fraction can be observed. A reason for this might be that the lack of solid volume suddenly appearing as larger particles are exchanged into smaller ones, is more evident as the number of large particles is low. Most of the solid volume is concentrated in the larger particles, and deleting a significant fraction of these will then create a large volume of void space needed to be compensated for by increasing all the particle radii in the structure in order to have a constant solid volume fraction. In the opposite end of the spectrum, where the size ratio approaches 1, switching sizes of particles does not have any significant effect, which is expected. If the particles are of the same size, a switch between the two types will be equivalent to no switch at all. The observed fluctuations are merely noise as a result of the randomness of the structures. In between the two extreme cases the dependence tends to be more linear, showing that the effect of changing particle sizes has a similar effect for all number fractions. A scaled comparison based on minimizing the sum of squared differences between permeability and squared mean pore size is found in Fig. 4.6. Again, the correspondence between the two quantities is evident.

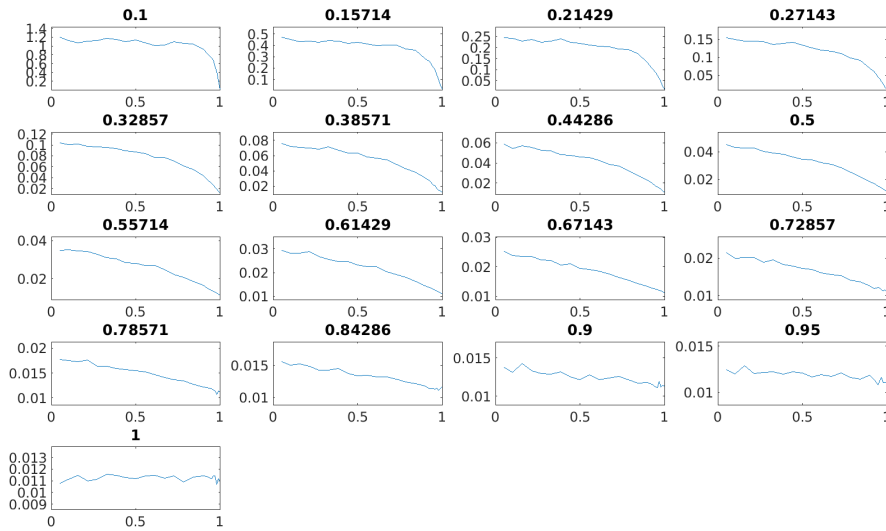


Figure 4.4: Permeability $[l^2]$ as a function of the number fraction (x-axes) of small particles plotted for all size ratios (captions) separately. The solid volume fraction is 0.50. Note that l is the problem-dependent proper length (see Sections 3.3.3 and 3.4.2)

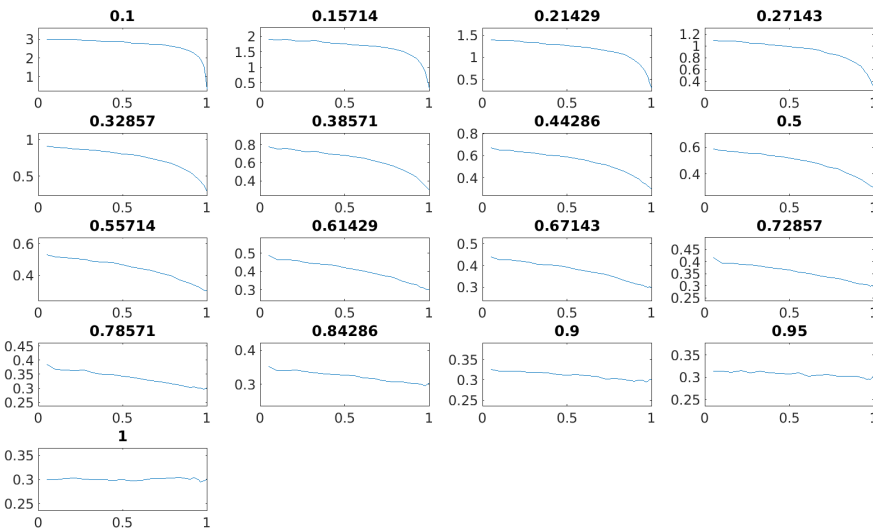


Figure 4.5: The mean pore size $[l]$ as a function of the number fraction (x-axes) of small particles plotted for all size ratios (captions) separately. The solid volume fraction is 0.50. Note that l is the problem-dependent proper length (see Sections 3.3.3 and 3.4.2).

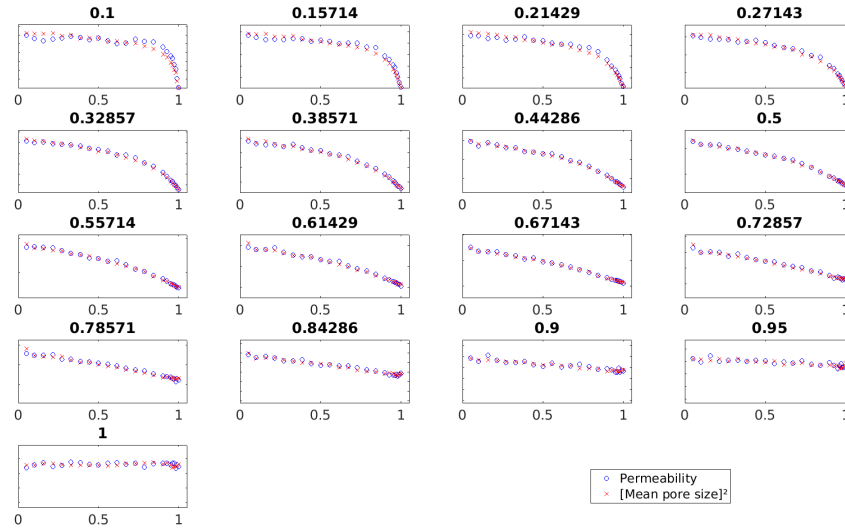


Figure 4.6: Comparison of permeability and squared mean pore size as a function of the number fraction (x-axes) of small particles plotted for all size ratios (captions) separately. The solid volume fraction is 0.50.

4.3 From lattice structures to random packings

A series of structures based on monodisperse size distributions, with solid volume fractions ranging between the maximum packing fraction $\Phi_{max} = \pi/\sqrt{18} \approx 0.7403$ to $\Phi_{min} = 0.63$, was generated using the lattice method described in Section 3.1.2. The resulting permeability and mean pore size are plotted in Fig. 4.7. A scaled comparison based on minimizing the sum of squared differences between permeability and squared mean pore size is plotted in Fig. 4.8. As can be seen, the assumption that there is a linear relation between the permeability and the squared mean pore size holds even for dense packings.

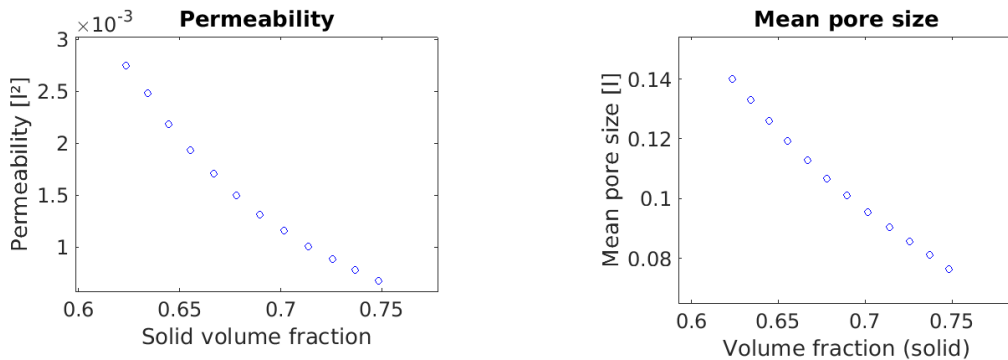


Figure 4.7: Permeability (left) and mean pore size (right) as functions of solid volume fraction. Note that l is the problem-dependent proper length (see Sections 3.3.3 and 3.4.3).

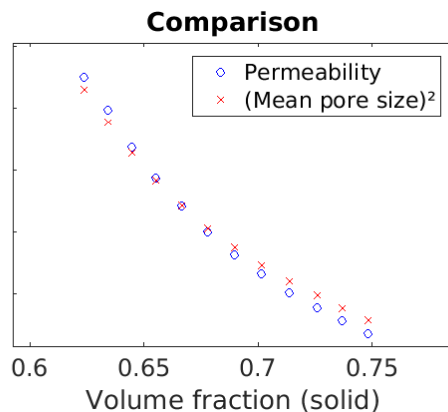


Figure 4.8: A comparison between the permeability and the squared mean pore size.

The two-point probability functions for the void phase for some of the solid volume fractions are calculated and plotted in Fig. 4.9. For a vanishing point separation, S_2 attains the value of the volume fraction of the void Φ_{void} , which corresponds to the expected behavior explained in Section 3.3.2. As the separation increases, S_2 starts to oscillate around the asymptotic values Φ_{void}^2 . In the example in Section 3.3.2, oscillations indicated correlations between the points. As can be seen in Fig. 4.9, the different structures seem to be approximately equally correlated, based on visual comparison of the oscillations. However, the S_2 curve seems to stretch as the solid volume fraction decreases, indicating that the correlation lengths tend to be longer for smaller solid volume fractions. This is not surprising, since all structures in the series start from an fcc structure, and the stretching of S_2 merely indicates that the lattice is expanding. The expansion pushes the starting positions of the particles away from each other as the solid volume fraction decreases.

Since the algorithm runs for a certain number of iterations, and no specific goal is to be achieved (minimizing interaction energy etc.), the order in the structures from the lattice state obviously remains to some extent. A reason why the structures resemble each other to such a degree might be because of the dense nature of the structures. There is simply no room for the particles to relocate enough to observe any substantial difference between the different volume fractions, with the exception of the increase in correlation length due to the expansion of the lattice. The maximum packing fraction obtained in RCP for a monodisperse size distribution was found to be around 0.63, which implicates a quite narrow span of position options for the relocating particles in the expanded lattice, especially for volume fractions above 0.63. Hence, this suggests that an increase in the number of iterations for which the particles are allowed to move might not have any large effect on the result.

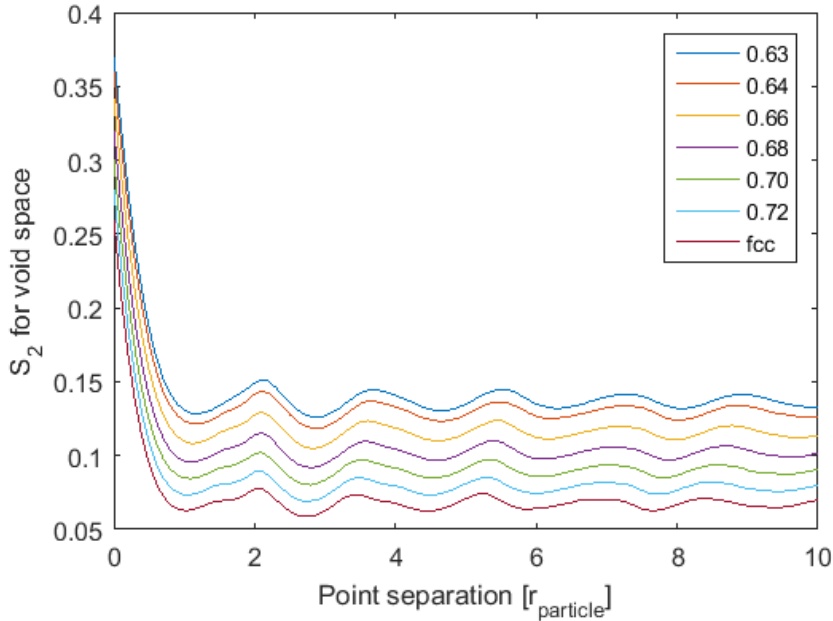


Figure 4.9: S_2 for the void phase as a function of the point separation for some different solid volume fractions.

An interesting comparison is between the two structures, with solid volume fraction 0.63, one obtained via RCP and the other obtained via the lattice method. The two-point probability function is plotted in Fig. 4.11 and a histogram of the pore sizes is found in Fig. 4.12. As can be seen, the structure obtained by the lattice method possesses longer-length correlations, in agreement with the analysis above. A visual comparison between the pore sizes in Fig. 4.12 indicates that the RCP structure seems to contain larger pores on average. The mean pore sizes are $0.1562 l$ for the RCP structure and $0.1402 l$ for the lattice method structure. Hence, the RCP structure, which approximately attains the largest possible value for an RCP (see Section 4.1), encloses void space inaccessible without any order in the configuration. Also, permeability is higher for the RCP structure ($0.0031 l^2$ compared to $0.0027 l^2$), which corresponds well to the above reasoning in Section 4.1 about the link between permeability and mean pore size. The two structures are illustrated in Fig. 4.10. As can be seen, despite the same solid volume fraction, the structures truly are different. The ordered nature of the structure obtained by the lattice method, as well as the high randomness in the structure obtained by RCP, is clearly visible. Hence, the different correlation lengths observable in Fig. 4.11 seems reasonable.

It might be concluded, though, that the lattice method does not generate typical semicrystalline structures, where some regions are random and other are ordered. The generated structures are rather perturbed lattices. Due to the lack of space needed for the particles to reconfigure, the crystalline part clearly dominates throughout the structures (since the particles more or less are locked in their positions). If the expansion of the lattice were continued, e.g. to a corresponding solid volume fraction 0.4, the particles would be given more space to utilize in the reconfiguration process. However, the random displacements introduced in the second stage

(after expanding the lattice) would jeopardize the crystalline part. Hence, the lattice method seems to either generate perturbed lattice structures (for denser packings) or structures similar to random packings (for looser packings). Hence, a suggested way to overcome the problem would be to create structures from crystalline and random substructures, generated separately.

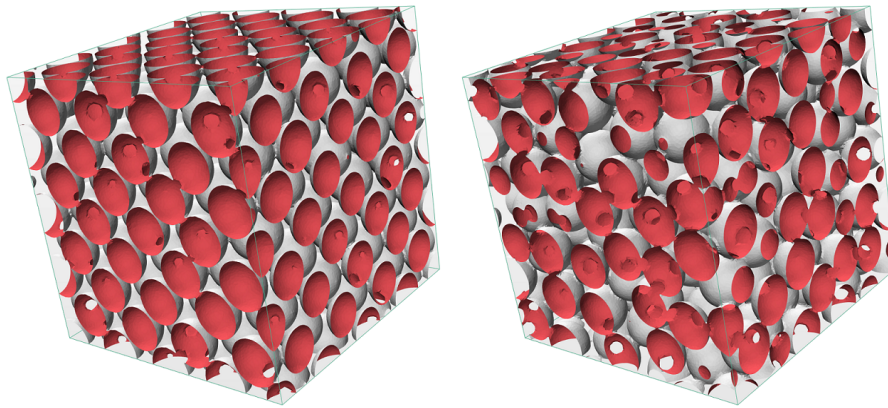


Figure 4.10: The structures obtained by the lattice method (left) and RCP (right).

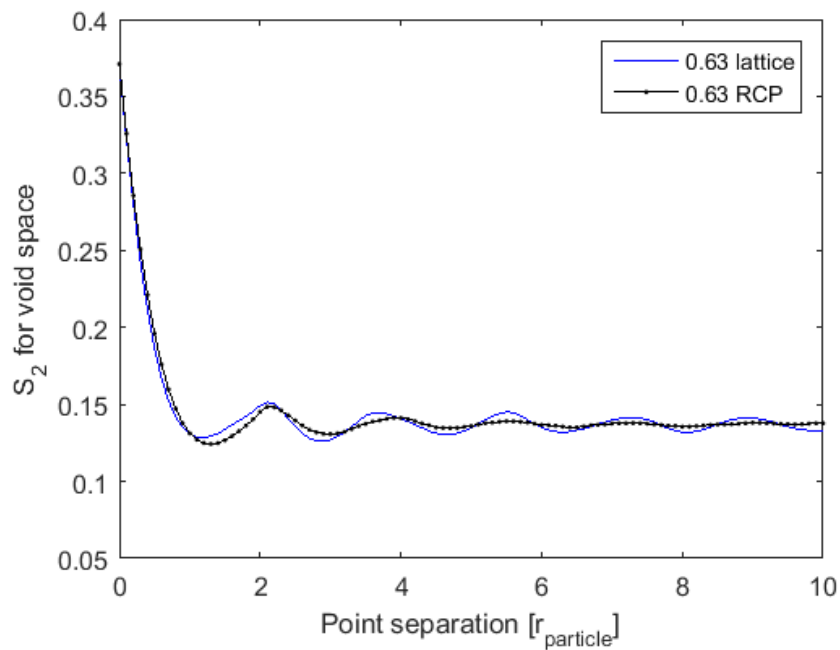


Figure 4.11: S_2 for the void phase as a function of the point separation for a solid volume fraction of 0.63, obtained by RCP and by the lattice method.

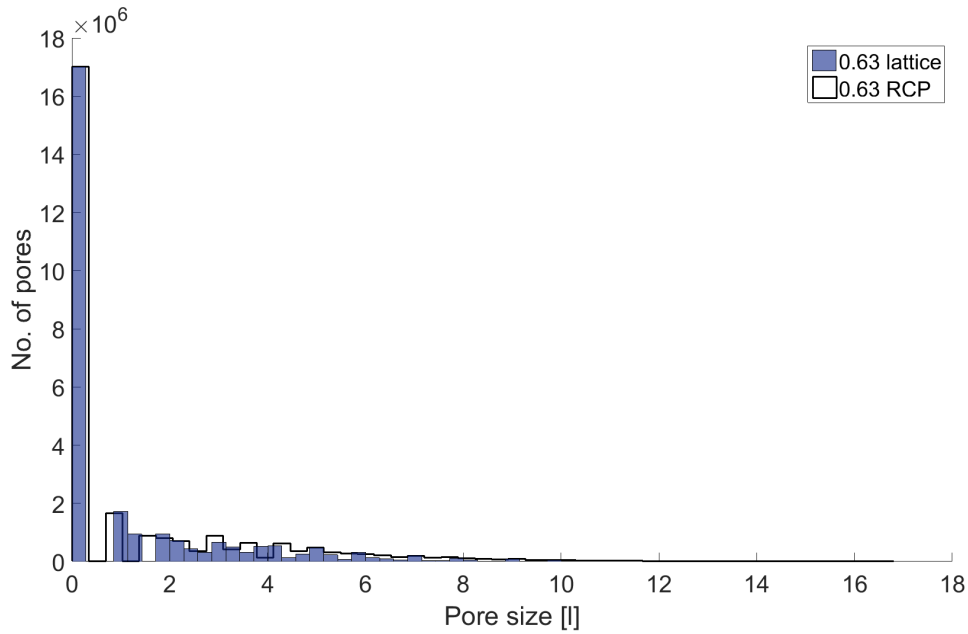


Figure 4.12: A comparison of the pore sizes for the two structures, obtained by RCP and by the lattice method. Note that l is the problem-dependent proper length (see Sections 3.3.3 and 3.4.3).

4.4 Investigation of effects related to spatial correlations

As mentioned in Section 3.1.3, to investigate the effect related to spatial correlations in the structures, only particle positions are changed, keeping the size distribution, and hence the solid volume fraction, porosity and specific surface constant. Different approaches were applied in order to force the particles to move to or avoid certain locations in the structure: (i) introducing forces between the particles, (ii) including repulsive point potentials in the structure, and (iii) deleting particles from a generated structure. The methods are described in Section 3.1.3.

4.4.1 Introducing forces between particles

The resulting permeabilities and mean pore sizes for the different cases of applied forces are found in Fig. 4.13. Comparisons between permeability and squared mean pore size are plotted in Fig. 4.14 separately. As can be seen, the permeability is affected by the performed modifications of the structures. The effect is large for lower volume fractions, which seems reasonable, because in denser structures, where the solid volume fraction is high, the particles are already packed close together, effectively decreasing the degrees of freedom. Applying any type of force between the particles to such a structure does not create any significant difference between the modified and the original structure. Hence, the impact of structure on permeability decreases with increasing solid volume fraction. A small fluctuating difference in permeability between the two cases, attractive and attractive + repulsive forces,

can be observed. This is probably an effect of noise caused by the random nature of the generating process of the structures.

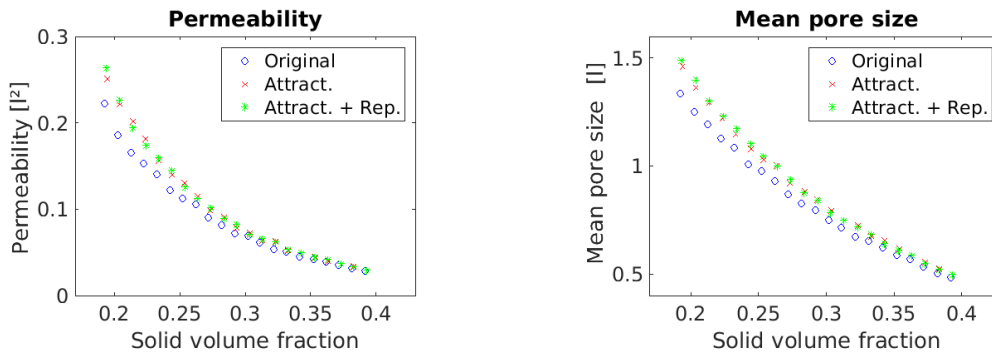


Figure 4.13: Permeability (left) and mean pore size (right) for the three different cases. Note that l is the problem-dependent proper length (see Sections 3.3.3 and 3.4.4).

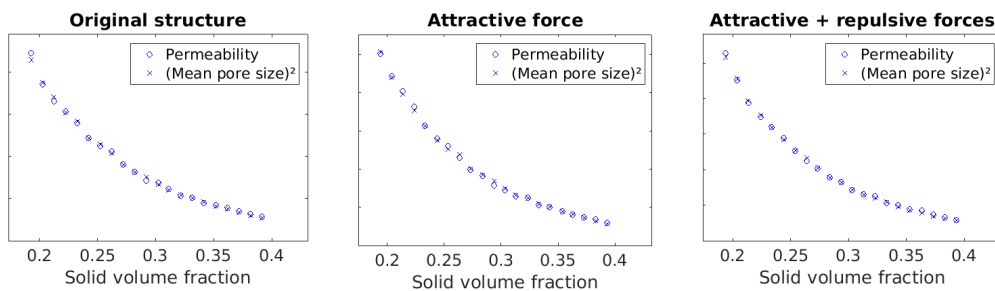


Figure 4.14: A scaled comparison based on minimizing the sum of squared differences between permeability and squared mean pore size.

S_2 for the void phase for the three cases for a solid volume fraction of 0.20 is plotted in Fig. 4.15. For a vanishing point separation, S_2 attains the value of the volume fraction of the void $\Phi_{void} = 0.80$, and for a large separation, S_2 attains the asymptotic value of $\Phi_{void}^2 = 0.64$, indicating that points separated on these distances are uncorrelated, as discussed in Section 3.3.2. The minima are corresponding to a separation of about one particle diameter. Interesting, though, are the minimum values of S_2 for the three cases, which differ. The smallest minimum value corresponds to the original structure, where no force is applied. The largest minimum value corresponds to the case where both an attractive and a repulsive force were applied between the particles. In between is the case corresponding to only an attractive force between the particles. Comparing this result to the example in Section 3.3.2, it seems like the cases, in which some kind of force has been applied, are in between the two extreme cases of overlapping and nonoverlapping particles. This intermediate state may be interpreted as that particles tend to create clusters. A possible reason for the shallower dip in the case of opposing forces, compared to only an attractive one, may be that particle clusters get pushed away from each other, due to the repulsive force acting on longer distances, which seems to have increased

the clustering effect. The stretching tendency of S_2 , similar to the one observed in Fig. 4.9 for the lattice method, is observed in Fig. 4.15 as well, which may be a result of the separation between particle clusters.

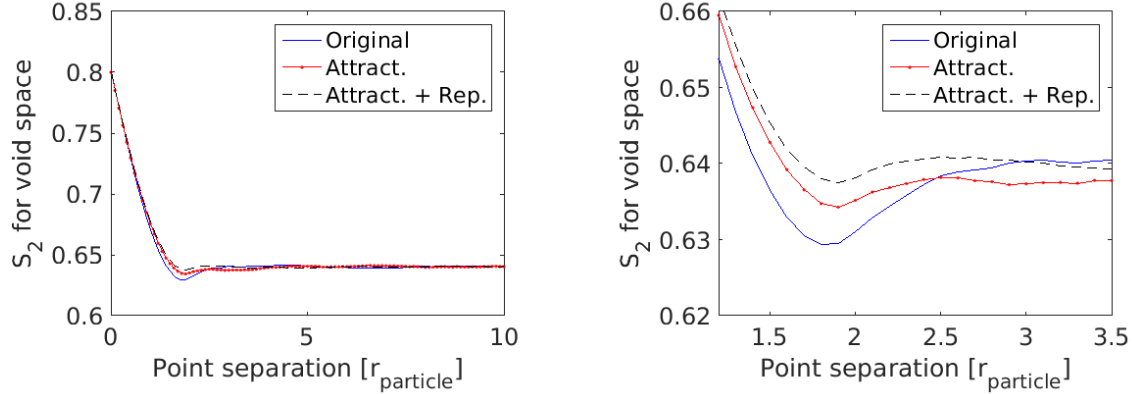


Figure 4.15: S_2 for the void phase for three cases (left) and a magnification of the minima (right). The solid volume fraction is 0.20.

A comparison between the mean pore sizes (Fig. 4.13) for solid volume fraction 0.20 shows that the mean pore size is larger for attractive + repulsive forces than for only an attractive force. This coincides with the analysis of S_2 above. For a solid volume fraction of 0.22, the mean pore size for the two cases of applied forces are almost equal. S_2 for the two cases is plotted in Fig. 4.16. As can be seen, the two curves now almost attain the same minimum, which is related to the similar mean pore sizes observed in Fig. 4.13. Permeability, on the other hand, is shifted between the two cases of solid volume fraction. This, however, is probably a noise effect related to the randomness in the generating process and in the structures, which might not be fully captured in the mean pore size and in S_2 .

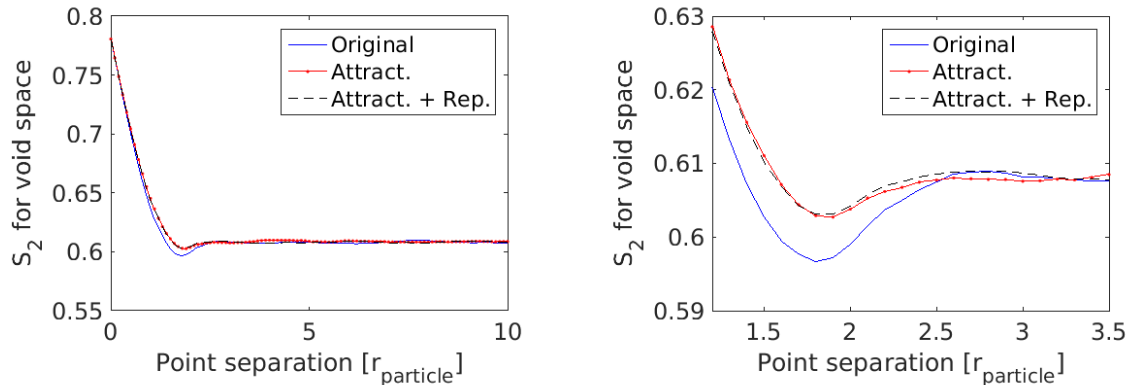


Figure 4.16: S_2 for the void phase for three cases (left) and a magnification of the minima (right). The solid volume fraction is 0.22.

As mentioned in Section 3.1.4, the voxelization in Matlab and the triangulation in VoxSurface affect the final structures used in the fluid dynamics simulations. For

example, particles located close to each other may in some cases be separated by a distance smaller than the discretization step, which results in a welding of the surfaces, as observed for the denser packings in Section 4.1. The more clusters in the structure, the greater the risk of getting an effect of the welding. By forcing the particles to create clusters may hence alter the specific surface and the volume fraction somewhat. The corresponding values on the specific surface are plotted in Fig. 4.17. Theoretically, the specific surface should be equal in all three cases for a certain solid volume fraction. However, the tendency toward lower values in the cases where forces have been introduced is a result of particle clusters and welding.

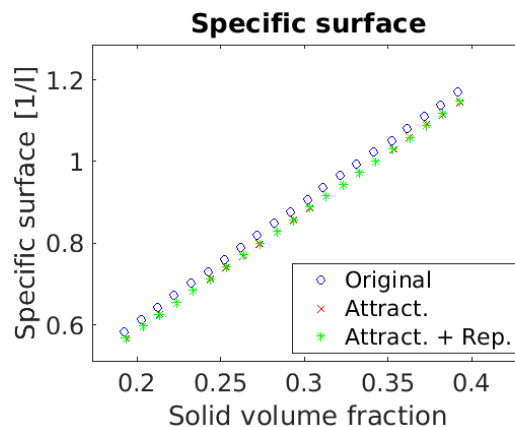


Figure 4.17: Specific surface as a function of the solid volume fraction for the original and the modified structures. Note that l is the problem-dependent proper length (see Sections 3.3.3 and 3.4.4).

4.4.2 Repulsive point potentials

The resulting permeability and mean pore size are plotted in Fig. 4.18. A comparison between the permeability and the squared mean pore size is plotted in Fig. 4.19. There seems to be large variations in permeability, both as a function of the solid volume fraction and as a function of the number of potentials. Similar to the case in Section 4.4.1, the significance of the repulsive potentials is larger for smaller volume fractions due to the larger fraction of void in these structures, meaning a greater translational freedom for the particles. A possible explanation to the large fluctuations may be the impact of the random positioning of the potentials. Since there is no counter force in the model, more than the condition that no overlaps should occur, the influence of a single potential on the particles may be very large. If potentials happen to be located very close to each other, there will only be a small region between them where they will oppose each other's effect on the particles. In the remaining domain, closely positioned potentials will work as one. The greater the distance between the potentials, the more significant their individual contributions will be. This effect seems to decrease somewhat with an increasing number of potentials. With a larger number of potentials, the chance for a wider spread of the potentials in the domain is increased.

The fluctuations are not as significant in the mean pore size, which tends to be fairly constant as a function of the number of potentials, and decreases as a

function of the solid volume fraction. Based on the scaled comparison in Fig. 4.19, it seems like the correspondence between the permeability and the squared mean pore size found in previous sections is no longer as evident. A comparison between structures where the correspondence between permeability and squared mean pore size are good and bad, respectively, is found in Figs. 4.20 - 4.21. As can be seen, as the number of potentials is low, their individual effect is larger. Since there is no counter force to the repulsive potentials, the particles will be pushed away from these regions, and the result is a large opening in the structure. The flow is in the x-direction, and as can be seen in the structure to the right hand side in Figs. 4.20 - 4.21, the particles form a wall in the yz-plane, creating a barrier for the fluid to pass through. This is the reason for the low permeability despite a relatively high value on the squared mean pore size. Hence, in cases where the structures are less isotropic, the assumption that the spatial correlations may be captured in the mean pore size alone is too much of a simplification.

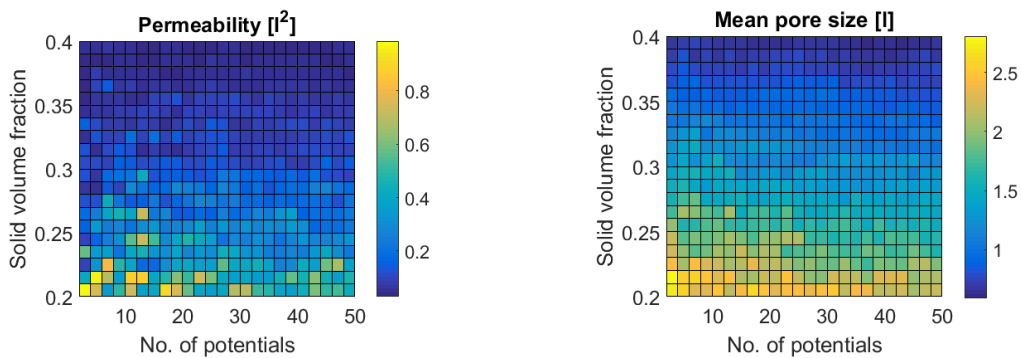


Figure 4.18: Permeability (left) and mean pore size (right) as functions of the number of repulsive potentials and the solid volume fraction.

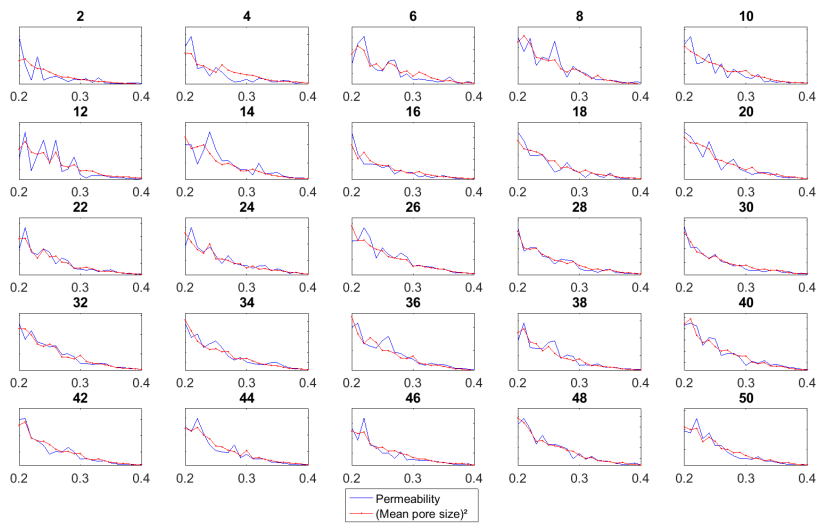


Figure 4.19: Comparison of the permeability and the squared mean pore size as a function of the solid volume fraction (x-axes) plotted separately for different number of repulsive potentials (captions). Note that l is the problem-dependent proper length (see Sections 3.3.3 and 3.4.4).

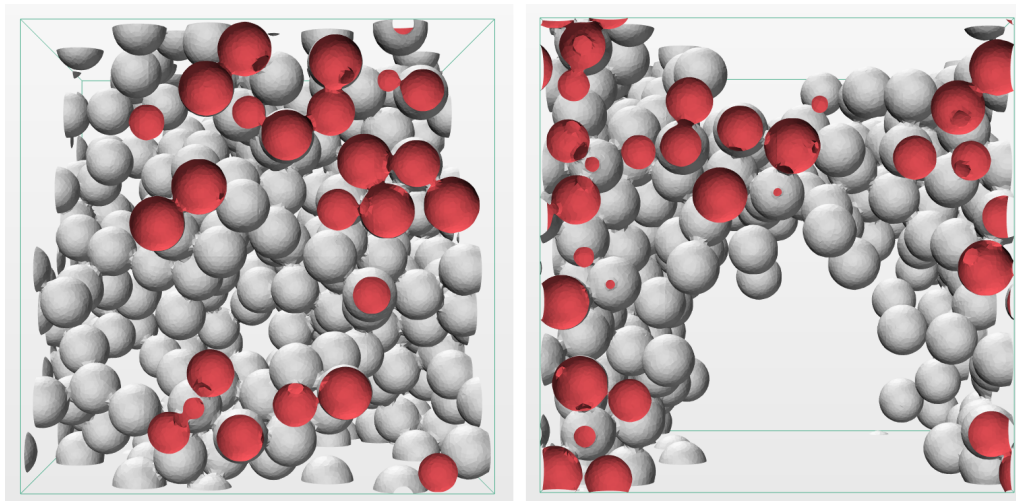


Figure 4.20: Comparison of two structures in the xy -plane for which the correspondence between the permeability and the squared mean pore size is good (left) and bad (right). The solid volume fraction is 0.22 in both cases, and the number of repulsive potentials is 48 (left) and 2 (right).

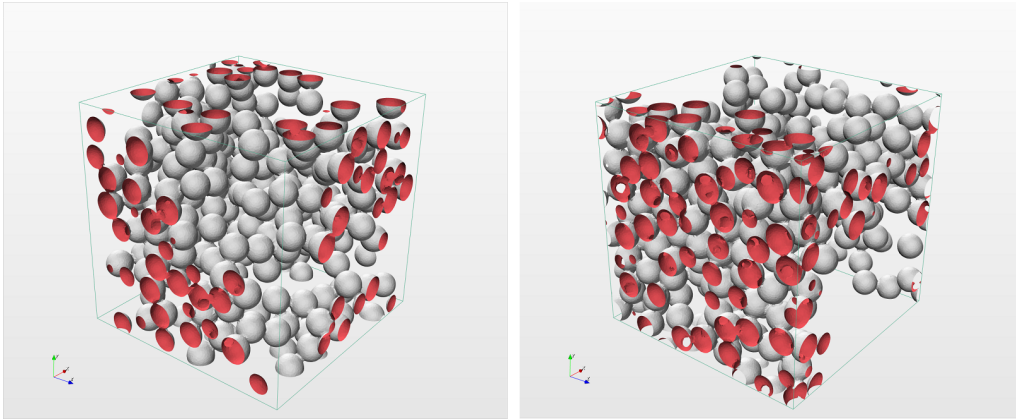


Figure 4.21: Same comparison as in Fig. 4.20, but from a different angle. The left structure produces a good correspondence and the right structure produces a bad correspondence. A clarification of the spatial orientation: x (red), y (green), z (blue).

S_2 for the two cases of structure is plotted in Fig. 4.22. In the interval $[0, 2r_{particle}]$, the curves follow each other, and both structures show a dip for a point separation around $2r_{particle}$. As the separation increases, S_2 decreases. As can be seen, the plain blue line corresponding to the anisotropic structure attains higher values than for the more isotropic structure. This indicates that the probability of successfully finding two points in void space is higher than in the anisotropic structure, which corresponds well to the open structure in Fig. 4.20 - 4.21.

To increase the number of particles used (and scale them to appropriate sizes to obtain the same solid volume fractions as before) while keeping the number of potentials unchanged, as an attempt to overcome the problem with creating anisotropic structures, would probably have a small, if any, effect on the result. The repulsive forces acts without any balance to other forces in the system (apart from the condition of nonoverlapping particles). Hence, particles, no matter the total number in the system, will be pushed away in a similar manner for similar solid volume fractions.

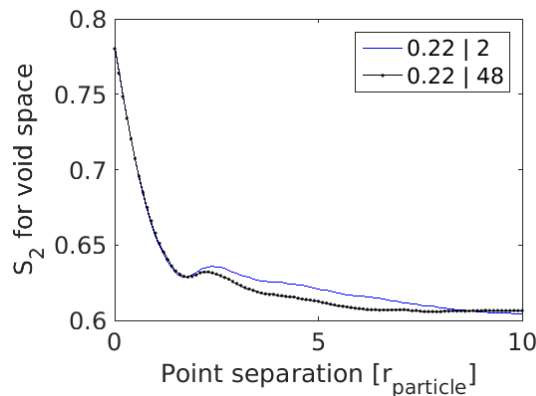


Figure 4.22: S_2 for the two structures in Fig. 4.20 - 4.21.

4.4.3 Deleting particles from the structure

The resulting permeability and mean pore size are plotted in Fig. 4.23. An investigation of the plots indicates that the permeability behaves in a similar irregular manner as in the previous case in Section 4.4.2, but not to the same degree. The resemblance between the cases holds for the mean pore size as well. Despite the irregularities, there is an observable trend tending to display a relation between the pore sizes and the permeability. The permeability and the squared mean pore size are plotted in Fig. 4.24. As can be seen, the linear relationship is weaker in cases where the influence on the structures are large, i.e. in the cases where either the size or the volume fraction of the deleted particles are large.

The resemblance between deleting particles from the structures and to introduce repulsive potentials is not surprising, though. The larger particles, like the repulsive potentials, are distributed randomly. Hence, it is possible that larger particles happen to be located close to each other, and deleting them would give rise to large void regions in the domain. The impact on the structure, however, is less significant. In contrast to the long range action of the repulsive potentials, the effect of deleting particles is only local. The risk of forcing the particles into wall formations can also be controlled via the size ratio and volume fraction of the larger particles. This type of mechanism is not achievable using unbalanced repulsive potentials, as in Section 4.4.2. Hence, it seems achievable to introduce some sort of control over the pore sizes, and have some manual influence of the structure, by deleting a portion of the particles from the domain. However, in order to obtain a more reliable and stable correlation between the permeability and the mean pore size (or squared mean pore size), a larger system needs to be taken under consideration, meaning a larger number of particles (of both sizes).

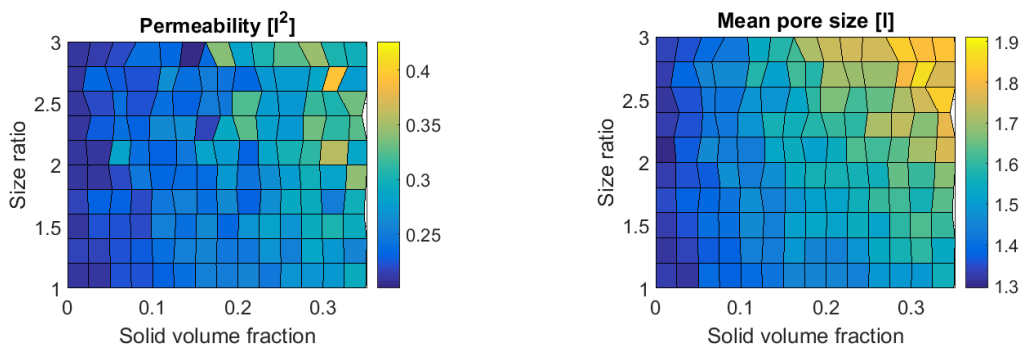


Figure 4.23: Permeability (left) and mean pore size (right) as functions of number of larger particles and size ratio between the larger and smaller particles and solid volume fraction of the larger particles. Note that l is the problem-dependent proper length (see Sections 3.3.3 and 3.4.4).

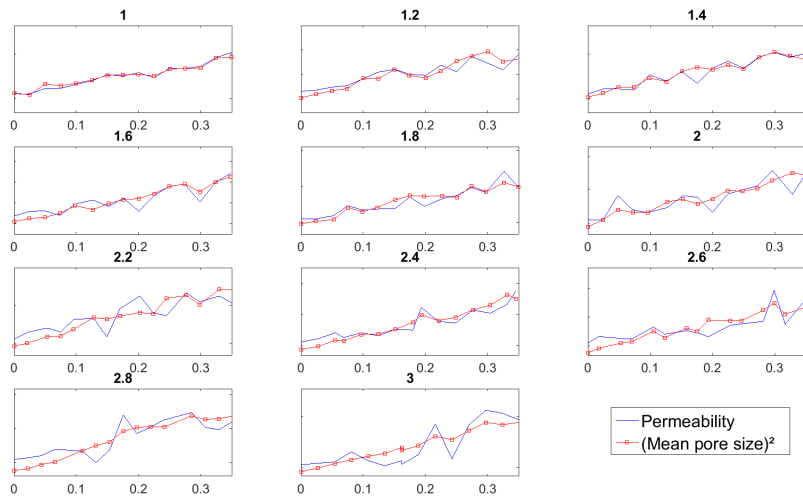


Figure 4.24: Comparison between the permeability and squared mean pore size as a function of the volume fraction of the larger particles, plotted separately for different size ratios.

4.5 The Kozeny-Carman equation

The version of the Kozeny-Carman equation including a dependence on the pore size distribution, Eq. (2.4) stated in Section 2.2, is provided once more:

$$\kappa = \tilde{C} f(\Lambda) \frac{\Phi_{void}^3}{S^2 (1 - \Phi_{void})^2}. \quad (4.2)$$

The results from the simulations strongly suggests that a there is a relationship between the squared mean pore size and the permeability, at least for isotropic structures. To reiterate, the generating method gives statistically isotropic structures. However, a particular realization may be highly anisotropic. Problems arise when the isotropy of the structures decreases, and for highly anisotropic structures, the choice of flow direction in the simulation becomes important. As can be seen in Fig. 4.20-4.21, the choice of direction is truly important for the structure on the right-hand side. As mentioned in Section 4.4.2, the flow was in the x -direction. However, the open structure would function as a canal in the z -direction. Hence, considerably different results would be expected if flow in the z -direction were to be considered instead. Some sort of quantification of the isotropy (or anisotropy), or a related property of the structure, would be preferable. This, however, will not be achievable during the time frame of this thesis, and hence, the effects of anisotropy will be neglected in the discussion. However, based on the results from the more isotropic structures it can be concluded that

$$f(\Lambda) = \Lambda^2, \quad (4.3)$$

where Λ is the mean pore size. A suggested version of the Kozeny-Carman equation would then take the form

$$\kappa = \tilde{C}\Lambda^2 \frac{\Phi_{void}^3}{S^2(1 - \Phi_{void})^2}. \quad (4.4)$$

The obtained exponent of Λ it is not obvious (e.g. from dimensional analysis), though, since \tilde{C} might have a unit as well. However, Λ^2 seems natural since permeability has unit of length² and the mean pore size has unit of length.

Now, using the earlier results from the Section 4.4.1, for which the relation between permeability and the squared mean pore size holds, a test of the assumption may be performed. For a specific volume fraction, the only difference between the three series is the particle positions. Hence, \tilde{C} in Eq. (4.4) should be the same. For the three cases, \tilde{C} is estimated by minimizing the sum of squared differences. The resulting constants are:

$$C_{org} = 0.005840; \quad C_{att} = 0.006048; \quad C_{att+rep} = 0.005982. \quad (4.5)$$

As can be seen, they are approximately equal. This strengthens the hypothesis that for isotropic structures, the permeability is a function of the squared mean pore size. The fact that there is a relationship between the two quantities is quite natural. A larger amount of empty space in the structure would reasonably permit a larger flow. A condition for a flow is, though, that the porous domains are connected. This is the case in the structures used, since the particles are not overlapping. If, however, overlapping particles were allowed in the structure, it would have been possible for porous domains to be isolated and not contribute to the transport of fluid through the structure.

5

Conclusion

It has been shown that permeability is affected by the particle size distribution. The permeability is larger for a polydisperse case compared the monodisperse case of the same solid volume fraction. The obtained mean pore sizes were larger in the polydisperse cases, which tentatively is the reason for the increased permeability. A more detailed analysis of the bidisperse size distribution was performed. However, a similar exhaustive investigation may be interesting for the lognormal distribution, as well, e.g. varying variance and solid volume fraction.

The size distribution affects the maximum packing fraction obtained by RCP, i.e. the packing fraction of structures of randomly distributed particles packed to a maximum possible density, as well. By using a polydisperse size distribution, denser packing fractions are possible, which coincides with previous experimental and theoretical results. The obtained maximum packing fraction for the monodisperse distribution was around 0.63, which is somewhat lower than previous published results. However, the maximum packing fraction is dependent on the size of the domain, and hence a larger number of particles would be needed to obtain denser packings. An interesting continuation would be to investigate the effects on RCP by changing the parameters in the distributions, e.g. size ratio and variance.

Different degrees of heterogeneity in the structures has been shown to affect the permeability. Attempts to control the pore sizes in the structures were performed using methods of different degree of physical relevance. An attractive force, in combination with or without any repulsive force, between the particles affects the clustering. Introducing repulsive point potentials at random positions in the domain is a rather unphysical approach, and without any counter force it is difficult to control the effect on the structures. When the number of potentials is low, the positions of the repulsive point potentials have substantial impact. This effect decreases somewhat as the number of potentials, as well as the solid volume fraction, is increased. A more reliable and realistic method seems to be to generate structures based on bidisperse size distributions, where one particle type is removed in the second stage. The pore sizes may be controlled by changing the number fraction and size of the particles to be removed. Hence, the risk of obtaining highly anisotropic structures, as the ones obtained using repulsive potentials, may be reduced by tuning these parameters. However, in order to fully evaluate the method, a larger number of particles is needed (tentatively of both kinds).

The combined result from changing the particle size distribution and from changing the degree of heterogeneity in the structures suggests that there is a linear relationship between the permeability and the squared mean of the pore size distribution. However, modifying the structures in order to obtain different degrees

of heterogeneity might affect the degree of isotropy in the structures. For highly anisotropic structures, the permeability becomes dependent on the flow direction, a feature not captured by the mean pore size. Possibly, computing the permeability as an average over all three flow directions may give more consistent results.

The two-point probability function was successfully used to investigate spatial correlations and order in structures, as well as to characterize clustering. Isotropic structures were assumed, and hence the dependence of the orientation of the points was neglected. However, this assumption does not hold for highly anisotropic structures, e.g. for modified structures where only a few repulsive potentials have been used. Despite an indication of highly anisotropic structures due to large void regions, the significant difference between isotropic and anisotropic structures is not captured to an appropriate degree by the isotropic version of the two-point probability function used. To not assume isotropy, and hence include a dependence on the orientation of the points, might provide some interesting results and is suggested as a possible continuation of the investigation.

Only spherical granules were studied in this thesis. In the continuation of the exploration of the space of material configurations, also particles of different shapes may be considered, e.g. ellipsoids or rods. Also allowing particles to overlap would introduce another dimension to the problem.

Bibliography

- [1] J. Patterson and B. Bernard. *Solid-State Physics. Introduction to the Theory*. Springer, second edition, 2010.
- [2] Lars Davidson. *Numerical Methods for Turbulent Flow*. Unpublished, 2005.
- [3] A. Satoh. *Introduction to Practice of Molecular Simulation*. Elsevier, 2011.
- [4] S. Torquato. *Random Heterogeneous Materials*. Springer Science + Business Media New York, 2002.
- [5] S. Curtarolo, G. L. W. Hart, M. Buongiorno Nardell, N. Mingo, S. Sanvito, and O. Levy. The high-throughput highway to computational materials design. *Nature Materials*, 12:191–201, February 2013.
- [6] M. Röding, E. Schuster, K. Logg, M. Lundman, P. Bergström, C. Hanson, T. Gebäck, and N. Lorén. Computational high-throughput screening of fluid permeability in heterogeneous fiber materials. *Unpublished*, 2016.
- [7] A. Belianinov, R. Vasudevan, E. Strelcov, C. Steed, S. M. Yang, A. Tselev, S. Jesse, M. Biegalski, G. Shipman, C. Symons, A. Borisevich, R. Archibald, and S. Kalinin. Big data and deep data in scanning and electron microscopies: deriving functionality from multidimensional data sets. *Advanced Structural and Chemical Imaging*, 2015.
- [8] O. Isayev, D. Fourches, E. N. Muratov, C. Oses, K. Rasch, A. Tropsha, and S. Curtarolo. Materials cartography: Representing and mining materials space using structural and electronic fingerprints. *Chemistry of Materials*, 27:735–743, 2015.
- [9] T. C. Lubensky. Soft condensed matter physics. *Solid State Communications*, 102(2-3):187–197, 1997.
- [10] R. P. Chapuis and M. Aubertin. *Predicting the Coefficient of Permeability of Soils Using the Kozeny-Carman Equation*. École Polytechnique de Montréal, 2003.
- [11] R. G. Holdich. *Fundamentals of Particle Technology*. Midland Information Technology and Publishing, 2002.
- [12] R. A. L. Jones. *Soft Condensed Matter*. Oxford University Press, 2002.
- [13] P. S. Liu and G. F. Chen. *Porous materials, Processing and Applications*. Butterworth-Heinemann (Elsevier), 2014.

- [14] F. A. L. Dullien. *Porous Media, Fluid Transport and Pore Structure*. Academic Press, second edition, 1992.
- [15] H. Darcy. *Les Fontaines Publiques de la Ville de Dijon*. 1856.
- [16] S. P. Neuman. Theoretical derivation of darcy's law. *Acta Mechanica*, 25: 153–170, 1977.
- [17] T. C. Hales. Cannonballs and honeycombs. *Notices of the AMS*, 47(4):440–449, April 2000.
- [18] G. Van Brummelen and M. Kinyon. *Mathematics and the Historian's Craft*. Springer Science + Business Media, Inc., 2005.
- [19] C. Kittel. *Introduction to Solid State Physics*. Wiley, eighth edition, 2005.
- [20] S. Torquato, T. M. Truskett, and P. G. Debenedetti. Is random close packing of spheres well defined? *Physical Review Letters*, 84(10):2064–2067, 2000.
- [21] G. D. Scott and D. M. Kilgour. The density of random close packing of spheres. *Journal of Physics D: Applied Physics*, 2(6):863–866, 1969.
- [22] K. W. Desmond and E. R. Weeks. Influence of particle size distribution on random close packing of spheres. *Physical Review*, August 2014.
- [23] H. Liasneuski, D. Hlushkou, S. Khirevich, A. Höltzel, U. Tallarek, and S. Torquato. Impact of microstructure on the effective diffusivity in random packings of hard spheres. *Journal of Applied Physics*, 116, 2014.
- [24] M. P. Ciamarra and A. Coniglio. Random very loose packings. *Physical Review Letters*, September 2008.
- [25] D.-H. Nguyen, E. Azéma, F. Radjai, and P. Sornay. Effect of size polydispersity versus particle shape in dense granular media. *Physical Review E*, 90, 2014.
- [26] A. V. Kyrylyuk and A. P. Philipse. Effect of particle shape on the random packing density of amorphous solids. *Physica Status Solidi A*, 208(10):2299–2302, 2011.
- [27] A. Donev, I. Cisse, D. Sachs, E. A. Variano, F. H. Stillinger, R. Connelly, S. Torquato, and P. M. Chaikin. Improving the density of jammed disordered packings using ellipsoids. *Science*, 303:990–993, February 2004.
- [28] D. Coelho, J.-F. Thovert, and P. M Adler. Geometrical and transport properties of random packings of spheres and aspherical particles. *Physical Review E*, 55 (2):1959–1978, February 1997.
- [29] H. K. Versteeg and W. Malalasekera. *An Introduction to Computational Fluid Dynamics*. Pearson Educational Limited, second edition, 2007.
- [30] Lars Davidson. *Fluid mechanics, turbulent flow and turbulence modeling*. Unpublished, 2016.
- [31] S. Succi. *The Lattice Boltzmann Equation*. Oxford University Press, 2001.

- [32] D. Hlushkou, H. Liasneuski, U. Tallarek, and S. Torquato. Effective diffusion coefficients in random packings of polydisperse hard spheres from two-point and three-point correlation functions. *Journal of Applied Physics*, 118, 2015.
- [33] T. Gebäck and A. Heintz. A lattice boltzmann method for the advection-diffusion equation with neumann boundary conditions. *Communications in Computational Physics*, 15:487–505, 2014.
- [34] C. R. Maurer, R. Qi, and V. Raghavan. A linear time algorithm for computing exact euclidean distance transforms of binary images in arbitrary dimensions. *IEEE Transactions on Pattern Analysis and Machine Intelligence*, 25(2):265–270, 2003.
- [35] V. S. Shumeiko. *Statistical Physics II (Statistical Physics of Non-Equilibrium Systems)*. Unpublished, 2009.

A

Appendix 1

A.1 Statistical mechanics

First, consider a system of N particles where particle i has position vector \vec{r}_i and momentum \vec{p}_i . For a three dimensional domain, a $6N$ -dimensional space consisting of the configurations of all the particles defines the phase space. A configuration of all the $6N$ variables, denoted in the compact form \vec{X} , defines a microstate of the system, with a corresponding energy $E(\vec{X})$. Using the energy given for the microstates, a probability density function, or distribution function, may be introduced:

$$f(\vec{X}, t) = \frac{\exp\{-E(\vec{X})/kT\}}{\int \exp\{-E(\vec{X})/kT\}d\vec{X}}, \quad (\text{A.1})$$

where k is Boltzmann's constant and T is the temperature [3, 35]. The denominator is the intergral over all microstates. The normalization ensures that

$$\int f(\vec{X}, t)d\vec{X} = 1 \quad (\text{A.2})$$

holds [35]. Since the system considered usually consists of a large number of particles, it is not (always) a convenient approach to keep track on microstates. Instead, a macrostate is defined, where properties such as pressure, temperature, and volume are considered, rather than particle positions and momentum. It is possible for a number of microstates to correspond to the same macrostate [35].